



## City Research Online

### City, University of London Institutional Repository

---

**Citation:** Yang, Y., Zhang, Y-Q. & Fu, F. (2024). Flexural behaviour of rectangular double-opening concrete filled sandwich steel tube (DCFSST) beams. *Journal of Constructional Steel Research*, 215, 108512. doi: 10.1016/j.jcsr.2024.108512

This is the accepted version of the paper.

This version of the publication may differ from the final published version.

---

**Permanent repository link:** <https://openaccess.city.ac.uk/id/eprint/32121/>

**Link to published version:** <https://doi.org/10.1016/j.jcsr.2024.108512>

**Copyright:** City Research Online aims to make research outputs of City, University of London available to a wider audience. Copyright and Moral Rights remain with the author(s) and/or copyright holders. URLs from City Research Online may be freely distributed and linked to.

**Reuse:** Copies of full items can be used for personal research or study, educational, or not-for-profit purposes without prior permission or charge. Provided that the authors, title and full bibliographic details are credited, a hyperlink and/or URL is given for the original metadata page and the content is not changed in any way.

---

---



# Flexural behaviour of rectangular double-opening concrete filled sandwich steel tube (DCFSST) beams

You-Fu Yang<sup>a,\*</sup>, Yu-Qin Zhang<sup>a</sup> and Feng Fu<sup>b</sup>

<sup>a</sup> State Key Laboratory of Coastal and Offshore Engineering, Dalian University of Technology, Dalian, 116024, China

<sup>b</sup> Department of Engineering, School of Science & Technology, City, University of London, Northampton Square, London, UK

**Abstract:** Experimental and numerical studies on flexural behaviour of rectangular double-opening concrete filled sandwich steel tube (DCFSST) beams were performed in this study. Six specimens under different cross-section of inner tube and nominal cross-sectional steel ratio ( $\alpha_n$ ) were tested under bending to assess the failure modes, moment-displacement and moment-strain relationships, flexural capacity and flexural stiffness of rectangular DCFSST beams. The experimental results demonstrate that the two design variables investigated in this paper have limited impact on the failure modes of typical specimens. The failure mode of outer tube includes multiple local bulges on top flange and one case of fracture on bottom flange that is located at the same plane as the primary local bulge on top flange, whilst the failure mode of inner tubes is mainly due to excessive global deflection. Simultaneously, sandwich concrete is crushed at the locations with evident local bulge on outer tube and cracks nearly uniformly within the lower 2/3 section depth. In general, the flexural capacity and stiffness of the specimens enhance as  $\alpha_n$  increases, and are moderately affected by the cross-section of inner tube. In addition, finite element (FE) models were built to replicate the flexural behaviour of rectangular DCFSST beams, and the FE models were validated by comparison with test results. At the end of the paper, simplified formulae that can better predict the flexural capacity of rectangular DCFSST beams were developed.

**Keywords:** Double-opening concrete filled sandwich steel tube (DCFSST); Rectangular section; Flexural behaviour; Tests; Finite element (FE) model; Simplified formulae.

\*Corresponding author. Tel.: 86-411-8470 8510; Fax: 86-411-8467 4141; E-mail address: youfuyang@163.com (Dr. You-Fu Yang).

## 1. Introduction

Replacing concrete core near the centroid of conventional regular concrete filled steel tube (CFST) by a hollow steel tube, i.e. the so-called concrete filled double-skin steel tube (CFDST), can reduce the amount of concrete and self-weight while maintaining good structural performance [1]. Compared with the CFST, the CFDST members have the characteristics of higher flexural stiffness, lighter self-weight and better dynamic load resistance due to their unique section form [2]. In the past two decades, the performance of CFDST structures under various loadings have received extensive attention, such as static behaviour and design method of members and joints [3-5], hysteretic performance and seismic design method of members, connections and frames [6-8], response and design calculation of members and joints under impact loading [9,10], fire performance of columns [11-13], among others. Large numbers of in-depth studies have significantly promoted the practical application of CFDST [1,2].

Nevertheless, for structural members to be used as hollow piers or towers, pipes on land and underwater, main structure of tunnels, etc. they are designed to withstand heavy loads requiring high stiffness and stability, the CFDST members cannot be directly employed or need to be retrofitted or reinforced before being adopted. To meet the above challenges, on the basis of previous studies, a new type of composite member was developed by the authors [14], i.e. rectangular double-opening concrete filled sandwich steel tube (DCFSSST), which evolves from the rectangular CFDST [15] and is formed from an outer steel rectangular hollow section (RHS), two inner steel tubes placed symmetrically within the infill concrete. Taking rectangular CFDST as a counterpart, the layout of inner tubes is more flexible for the rectangular DCFSSST, the inner tubes, for example, can be placed further away from the centroid after a rational arrangement, resulting in greater flexural capacity and flexural stiffness. Given the unique cross-sectional configuration, the rectangular DCFSSST is more suitable for members or structures that functionally need double holes, such as piers, bridge towers, principal body of two-way tunnels, etc.

Until now, there has been a certain amount of research on the flexural properties of CFDST with outer rectangular and square steel section. The first experimental and theoretical study on the flexural behaviour of CFDST beams with outer and inner steel square hollow section (SHS) was conducted by Zhao and Grzebieta [1]. After that, the flexural behaviour of CFDST members with the similar and different cross-sections of the tube received further attention, such as the CFDST beams with outer steel SHS and inner steel circular hollow section (CHS) [16], the CFDST beams with outer and inner steel RHS [15], and the CFDST beams with outer and inner steel SHS [17]. Additionally, the available studies on the flexural behaviour of CFDST also included members with pairs of concentric steel SHS and sandwich grout under blast loading [18], and members with outer SHS and inner CHS after exposure to high temperatures [19]. Currently, the only research on the newly proposed composite member concerning the experimental and numerical study of rectangular DCFSSST short columns under concentric compression has been carried out by the research group of reference [14].

The previous literature review shows that the investigation into the structural performance of rectangular DCFSSST members is very limited and there is almost no research on the flexural properties of rectangular DCFSSST beams. To provide theoretical basis for the flexural resistance design and thus facilitate engineering application of this new type of composite members, it is very crucial to understand their flexural behaviour. Hence, the goals of the present study are (1) to present the experimental results of 6 rectangular beams loaded in flexure, (2) to analyze the effect of the cross-section of the inner tube and nominal cross-sectional steel ratio on the flexural behaviour of the specimens, (3) to introduce the FE models that simulate the flexural behaviour of the rectangular DCFSSST beams and (4) to propose an accurate simplified model for the flexural capacity of the new composite beams.

## 2. Experimental study

### 2.1 Preparation of specimens

A total of six rectangular DCFSSST beam specimens, 3 with inner SHSs and 3 with inner CHSs, were designed and manufactured, and the cross-sections of the two inner tubes in each specimen were

identical. Fig. 1 shows the configuration of the rectangular DCFSSST beams, where  $D_o$ ,  $B_o$  and  $t_o$  are the depth, width and wall thickness of the outer steel RHS, respectively,  $d_i$  and  $t_i$  are the width or diameter and wall thickness of the inner steel sections, respectively, and  $d_e$  is the centroidal distance between the two inner tubes.

The main test parameter of the specimens was the cross-section of the inner tube and the nominal cross-sectional steel ratio,  $\alpha_n$ . The details of the specimens are presented in Table 1, where,  $\phi$  is the void ratio,  $e_0$  is the offset ratio of inner steel tube,  $f_{yo}$  and  $f_{yi}$  are the yield strengths of the outer and inner steel tubes,  $f_{cu}$  is the compressive cube strength of the sandwich concrete,  $M_{u,e}$  and  $K_{i,e}$  are the flexural capacity and flexural stiffness, and ‘S’ and ‘C’ in the labels denote that the cross-section of the inner steel tube is square or circular, respectively. The length (including two endplates) of the specimens ( $L$ ) was set to be 1200 mm.

The definition of  $\alpha_n$ ,  $\phi$  and  $e_0$  in the rectangular DCFSSST is as follows [14,15]:

$$\alpha_n = \frac{A_{so}}{A_{ceq}} \quad (1)$$

$$\phi = \sqrt{\frac{\sum A_{ssi}}{A_{ceq}}} \quad (2)$$

$$e_0 = \frac{d_e}{D_o} \quad (3)$$

where,  $A_{so}$  is the cross-sectional area of outer steel RHS;  $A_{ceq}$  is the equivalent cross-sectional area of concrete, that is, the cross-sectional area surrounded by the inner wall of outer steel RHS; and  $\sum A_{ssi}$  is the sum of cross-sectional area surrounded by the outer wall of inner steel tubes.

The outer RHSs were produced by welding together two identical cold-formed C-profiles with straight welds, while the inner SHSs and CHSs were fabricated from the finished cold-formed steel tubes. For all the specimens, the dimensions of two rectangular endplates were: depth×width×thickness=220 mm×160 mm×15 mm. The detailed fabrication process of rectangular DCFSSST beam specimens is the same as that of composite short columns in [14].

The properties measured for the steel tubes in the tensile tests of standard test coupons are listed in Table 2. The characteristic compressive cube strength of the sandwich concrete, measured in cubes with a side length of 150 mm, was designed as 40 MPa and its mix proportion includes: ordinary

108 Portland cement (P.O 42.5) 398 kg/m<sup>3</sup>, fly ash (grade I) 170 kg/m<sup>3</sup>, fine aggregate (river sand) 770  
1109 kg/m<sup>3</sup>, coarse aggregate (limestone gravel) 795 kg/m<sup>3</sup>, tap water 219 kg/m<sup>3</sup>, and water reducer 6.0  
2  
3  
1410 kg/m<sup>3</sup>. The measured properties of concrete include:  $f_{cu,28}$ =40.5 MPa,  $f_{cu}$ =49.8 MPa, and  $E_c$ =32.1  
5  
1611 GPa, in which  $f_{cu,28}$  is the compressive cube strength at the age of 28 days, and  $E_c$  is the elastic  
7  
8  
1912 modulus.

## 1113 2.2. Testing set-up and measurement

12  
13  
1414 Four-point bending tests were conducted to investigate the flexural behaviour along the major axis of  
15  
1615 rectangular DCFSSST beam specimens, and the vertical concentrated force monitored by a load cell  
17  
1816 was applied by a 5000 kN capacity testing machine and distributed to the two quarter points on the  
19  
20  
2117 top surface of the specimens by a spreader beam. Fig. 2 presents the testing set-up and it is seen that  
22  
2318 the effective span length  $L_e$  of the specimens is 1000 mm.

24  
25  
2619 A hybrid force & displacement control loading scheme was used in the tests. Prior to reaching the  
27  
2820 load corresponding to 90 % of the estimated ultimate value  $P_u$ , the force control rate of 0.5 kN/s was  
29  
30  
3121 employed, keeping the load constant at the levels of  $P_u/10$  about 2 to 3 minutes. After that the  
32  
3322 displacement control of the mid-span with the rate of 0.5 mm/min was adopted and each displacement  
34  
35  
3623 level of 5 mm in the mid-span was also held for 2 to 3 minutes. The tests were terminated, when the  
37  
3824 tensile area of the outer steel section fractured or the displacement in the mid-span reached approx.  
39  
40  
4125  $L_e/12$ .

42  
4326 To trace the development of deformations in the key positions of the specimens, five displacement  
44  
4527 transducers, DTs, were arranged as presented in Fig. 2(a), two at the supports, two at the quarter  
46  
47  
4828 points and one at the mid-span. Several longitudinal and transverse strain gauges, SGs, were attached  
49  
5029 on the outer walls of the outer and inner steel tubes in the mid-span, as shown in Fig. 2(b).

## 5130 2.3. Test results and discussion

### 54 55 5631 2.3.1. Failure modes

57  
5832 The test results indicated that, good deformability was achieved for all the specimens, considering  
59  
6033 that the displacement in the mid-span eventually reached 6% to 9% of  $L_e$ . The overall failure modes

of rectangular DCFSSST beam specimens are similar, that is, there are one primary local bulge on top flange and adjacent part of sidewalls as well as two secondary local bulges just on top flange of outer steel RHS within two quarter points, and one case of fracture on bottom flange and adjacent part of sidewalls of outer steel RHS that locates at the same plane as the primary local bulge; however, the final deflection shape, positions of local bulges and fracture site of outer steel RHS show a certain discrepancy for each specimen. Fig. 3(a1) shows the overall appearance of the specimens after the end of the tests, where the arrows point to the positions of the local bulges on the outer tube, and the dashed coils denote the fracture site of outer tube. The distance between the fracture site of outer tube and the mid-span section is approximately equal to  $B_o$ .

After removal of the outer steel tube, the failure mode of the sandwich concrete is displayed in Fig. 3(a2) and fine cracks of the length of approx.  $2/3$  of the section depth are uniformly distributed in the tension zone of all the specimens. Moreover, in the places where the evident localized bulge of outer tube occurs, the sandwich concrete is crushed, and the more obvious the localized bulge of outer tube, the greater the range and the higher the degree of concrete crushing.

Fig. 3(a3) demonstrates the failure mode of inner tubes and as seen in the figure, the failure in both of the inner tubes is mainly due to the global deflection and at the position of the outer tube with the local bulge, the inward local buckling appears in the upper inner tube of all the specimens with inner SHSs and one specimen with inner CHSs, since the CHS tubes have a better local stability as compressed than the SHSs that have a similar value of  $d_i/t_i$ , whilst the mid-span displacement of specimen RC-c is the largest among the three specimens with inner CHSs.

### 2.3.2. Moment versus deformation curves

Fig. 4 presents the experimental curves for the bending moment  $M$  vs. mid-span displacement  $u_m$  behaviour, where the hollow circles denote the flexural capacity and the relevant mid-span displacement, and the inverted triangles indicate the initiation of the fracture, ITF, at the bottom flange of the outer steel section. All the  $M - u_m$  diagrams consist of three successive phases that are categorized as approximate elastic, elasto-plastic and plastic hardening ones and the third phase



ends soon after the ITF. Moreover, while the cross-sections of the inner tubes are identical, a larger value of  $\alpha_n$  causes a higher slope at each phase of the  $M - u_m$  curve and a later appearing ITF. Simultaneously, when the section sizes of inner tubes and  $e_0$  are similar, the  $M - u_m$  curve of the specimens with inner SHSs is slightly higher than that of the specimens with inner CHSs, i.e. the former type has a better flexural performance.

The distribution of displacements  $u$  along the effective span can be determined on account of the data from all of the DTs in Fig. 2(a) as exhibited in Fig. 5 by the solid lines, and the relevant half-sine curves having the same  $u_m$  as the measured results are indicated by the dashed lines, where  $x$  is the distance from the fixed support to the measuring points, and  $m$  is the ratio of  $M$  to flexural capacity as defined later on. When  $m \leq 1.0$ , the measured displacements and the respective half-sine distribution are generally in good agreement, and there is a certain deviation between them while  $m > 1.0$ . In addition, for the same specimen, the deflection at the half span at the moment of the fracture in the outer tube is greater than that in the case without the fracture of the outer tube due to the concentration of the damage in the fracture.

Fig. 6 shows the recorded relationship between strains  $\varepsilon_L$  and  $\varepsilon_T$  in the mid-span and bending moment  $M$ , where the subscripts ‘L’ and ‘T’ stand for ‘longitudinal’ and ‘transverse’, respectively, and  $\varepsilon_{yi}$  is the yield strain of inner steel tube. The measured results indicate that, for the flange of outer steel RHS, the strains in the corner points 1-1 and 3-1 and in the middle points 1-2 and 3-2 are very close to each other and therefore only the values from the latter are presented. Figs. 6(a) and 6(c) indicate that in all of the specimens, the  $M - \varepsilon_L$  curve of the top flange of point 1-2 in the top flange has a similar development pattern, but there is a certain difference in the respective  $M - \varepsilon_L$  curve of point 3-2 of the bottom flange of the outer tube. This may be due to the difference in the width and length of concrete cracks near the mid-span section. According to the method of reference [16], the flexural capacity  $M_{u,e}$  of the rectangular DCFSSST beams is defined as the bending moment that causes strain  $\varepsilon_L$  equal to 0.01 at the bottom flange of the outer tube and the respective results are presented in Table 1. In general, strains  $\varepsilon_L$  in points f and g of the lower inner tube increase

continuously, whereas the values of  $\varepsilon_L$  in points d and e of the upper inner tube increase to a certain extent but then decrease while the neutral axis of the composite beam shifts gradually upwards during loading and thereafter downwards [20]. When bending moment  $M_{u,e}$  indicated by the hollow circle is reached, strains  $\varepsilon_L$  at points d, f and g of the inner tube are generally higher than  $\varepsilon_{yi}$ , and  $\varepsilon_L$  at point e of the inner tube is slightly less than  $\varepsilon_{yi}$ , indicating that the whole section of the lower inner tube and part of the upper inner tube have yielded and this is different from the yielding behaviour of the inner tubes in the rectangular CFDST beams [15-17]. It is shown in Figs. 6(b) and 6(d) that the  $M - \varepsilon_T$  diagrams have generally similar development patterns with the  $M - \varepsilon_L$  curves. Moreover, due to the Poisson effect, the absolute value of  $\varepsilon_T$  is smaller than that of the corresponding  $\varepsilon_L$  under the same moment.

The distribution of longitudinal strains  $\varepsilon_L$  is drafted on account of all the measurement results presented in Fig. 2(b) and the typical output until reaching moment  $M_{u,e}$  is presented in Fig. 7, where  $y$  indicates the vertical location of the point considered from the centroidal axis. It can be seen that, while  $m \leq 0.8$ , a linear distribution along the section depth is reached for the  $\varepsilon_L$  of both outer and inner tubes, and the location of neutral axis determined by the distribution of  $\varepsilon_L$  of outer steel RHS is generally the same as that determined by the distribution of  $\varepsilon_L$  of inner tubes. However, when  $m > 0.8$ , the distribution of  $\varepsilon_L$  is no longer linear in both outer and inner tubes, due to the occurrence of cracking of sandwich concrete and local bulge of the walls in outer tube. Additionally, the cross-sectional form of inner tubes has no obvious effect on the distribution of  $\varepsilon_L$ , whilst the larger the  $\alpha_n$ , the closer the neutral axis is to the centroid axis, meaning that increasing  $\alpha_n$  can enhance the confinement effect of outer tube on the sandwich concrete, and inhibit the upward shifting of neutral axis to a certain extent such that the damage process of the specimens slows down.

### 2.3.3. Mechanical index

The values of flexural capacity  $M_{u,e}$  are compared in Fig. 8(a) and it is seen that when  $\alpha_n$  is the same and the inner tubes have similar sizes and  $e_0$ , the specimens of RS series have similar values of  $M_{u,e}$  with the specimens of RC series and when  $\alpha_n$  has values 0.08, 0.113 and 0.147, the ratio

of capacities  $M_{u,e}$  between RS series and RC series is equal to 1.004, 1.071 and 0.974, respectively.

Simultaneously, with the same features of the inner tubes,  $M_{u,e}$  improves with the increasing  $\alpha_n$ .

For the RS series specimens, when  $\alpha_n$  is equal to 0.110 and 0.142,  $M_{u,e}$  is 20.6% and 51.0% higher than the respective values when  $\alpha_n = 0.079$ , whereas for the RC series specimens the similar percentage values are 13.0% and 55.6%, respectively. These effects follow mainly from the improved confinement of the outer tube to the sandwich concrete when  $\alpha_n$  increases.

The curvature of mid-span section can be acquired according to the assumption that the overall deflection of the specimens conforms to the half-sine curve form, which has been basically confirmed by the aforementioned discussion. The flexural stiffness  $K_e$  of the specimen at the elastic phase is equal to the ratio between the bending moment and curvature [15] and the values are listed in Table 1. The values of  $K_e$  are compared in Fig. 8(b) and it is seen that the values of  $K_e$  in the RS series are higher than those of the RC series, excluding the case with  $\alpha_n = 0.110$ . When  $\alpha_n$  varies from 0.079 to 0.142, the values of  $K_e$  in the RS series of specimens are 1.104, 0.930 and 1.042 times those of the specimens in the RC series. When the sizes and  $e_0$  of the inner tubes are kept unchanged, a larger value of  $\alpha_n$  results in a greater value of  $K_e$ . In the specimens of the RS series, when  $\alpha_n$  is equal to 0.110 and 0.142,  $K_e$  is respectively 11.2 % and 40.9 % higher than that when  $\alpha_n = 0.079$ , whereas in the specimens of the RC series the respective values are 32.0 % and 49.4 %. Clearly the increase of the stiffness of the inner tubes is the main reason for the improved values of  $K_e$  in the specimens of RS series.

According to references [20, 21], the flexural stiffness of CFST and CFDST members with rectangular cross-sections can be evaluated applying the superposition principle and the contribution of the concrete as cracked is close to 20 %. This principle is also applied when evaluating  $K_c$  for the rectangular DCFSSST beam specimens in Eq. (4):

$$K_c = E_{so} \cdot I_{so} + 0.2E_c \cdot I_c + \sum(E_{si,i} \cdot I_{si,i}) \quad (4)$$

where  $E_{so}$  and  $E_c$  are the elastic moduli and  $I_{so}$  and  $I_c$  are the moments of inertia for the steel tube and sandwich concrete, respectively and  $E_{si,i}$  and  $I_{si,i}$  are the elastic modulus and moment of

inertia for the inner steel tube  $i$ , respectively. The results show that, the minimum and maximum values of the ratio of  $K_c$  to  $K_e$  are 0.998 and 1.101, respectively, while its mean value and Cov are 1.062 and 0.040, respectively, which means that the flexural stiffness of rectangular DCFSSST beams can be well predicted in accordance with the superposition principle while considering 20% contribution of sandwich concrete, and overall the prediction is slightly higher than the test result.

### 3. Simulations by FE model

#### 3.1. FE models

The simulations for the flexural behaviour of the rectangular DCFSSST beams were carried out using the FE package ABAQUS [23] and the reliability of the evaluations was validated against the experimental results. The numerical analysis of typical rectangular DCFSSST beams was further performed by the FE model.

The behaviour of outer and inner steel tubes in ABAQUS was modelled as elasto-plastic material and the measured values for elastic modulus and Poisson's ratio were applied and the data pairs of real stress and plastic strain were transformed from the engineering values  $\sigma_s$  and  $\varepsilon_s$  to depict the plastic properties of steel materials. The  $\sigma_s - \varepsilon_s$  relationship for the cold-formed steel RHS and SHS proposed in [24] was adopted for the steel tubes, which contain 4 flat portions and 4 corner portions considering the local strengthening of corner area. The relationship between  $\sigma_s$  and  $\varepsilon_s$  of flat portions in the cold-formed rectangular and square steel tube is as follows:

$$\sigma_s = \begin{cases} E_s \cdot \varepsilon_s & (\varepsilon_s \leq \varepsilon_{s0}) \\ 0.75f_y + 0.5E_s \cdot (\varepsilon_s - \varepsilon_{s0}) & (\varepsilon_{s0} < \varepsilon_s \leq \varepsilon_{s1}) \\ 0.875f_y + 0.1E_s \cdot (\varepsilon_s - \varepsilon_{s1}) & (\varepsilon_{s1} < \varepsilon_s \leq \varepsilon_{s2}) \\ f_y + 0.005E_s \cdot (\varepsilon_s - \varepsilon_{s2}) & (\varepsilon_s > \varepsilon_{s2}) \end{cases} \quad (5)$$

where,  $E_s$  is the elastic modulus,  $f_y$  is the yield strength,  $\varepsilon_{s0} = 0.75f_y/E_s$ ,  $\varepsilon_{s1} = \frac{4}{3}\varepsilon_{s0}$ , and  $\varepsilon_{s2} = 3\varepsilon_{s0}$ .

The corner portions in the cold-formed rectangular and square steel tube are assumed to have the same expression for the  $\sigma_s - \varepsilon_s$  relationship as the flat portions; but yet the improved yield strength of the former in comparison with that of the latter was related to the yield-to-tensile strength ratio and

the corner radius to thickness ratio [24], and the corner radius in the cold-formed rectangular and square steel tubes was determined as suggested in reference [25].

The following five-phase constitutive model, which has been widely used in the previous FE simulations of composite members [29], was chosen to replicate the  $\sigma_s - \varepsilon_s$  relationship of inner steel CHSs:

$$\sigma_s = \begin{cases} \frac{E_s \cdot \varepsilon_s}{-A \cdot \varepsilon_s^2 + B \cdot \varepsilon_s + C} & (\varepsilon_{se} < \varepsilon_s \leq \varepsilon_{sa}) \\ f_y & (\varepsilon_{sa} < \varepsilon_s \leq \varepsilon_{sb}) \\ f_y \cdot (1 + 0.6 \frac{\varepsilon_s - \varepsilon_{sb}}{\varepsilon_{sc} - \varepsilon_{sb}}) & (\varepsilon_{sb} < \varepsilon_s \leq \varepsilon_{sc}) \\ 1.6f_y & (\varepsilon_s > \varepsilon_{sc}) \end{cases} \quad (6)$$

where,  $\varepsilon_{se}=0.8 f_y/E_s$ ,  $\varepsilon_{sa}=1.5\varepsilon_{se}$ ,  $A = 0.2 f_y/(\varepsilon_{sa} - \varepsilon_{se})^2$ ,  $B = 2A \cdot \varepsilon_{sa}$ ,  $C = 0.8f_y + A \cdot \varepsilon_{se}^2 - B \cdot \varepsilon_{se}$ ,  $\varepsilon_{sb}=15\varepsilon_{se}$ , and  $\varepsilon_{sc}=150\varepsilon_{se}$ .

The ductile damage model for metal in ABAQUS was selected to replicate the fracture process of steel tube, and there were two parameters of fracture strain and plastic damage factor that need to be defined. When the equivalent plastic strain of the element accumulated to the fracture strain, which was determined by the formulae provided in reference [26], the damage evolution began, and the linear damage criterion in reference [27] was subsequently adopted while defining the displacement at failure as the product of the average elongation and the standard distance of the coupons. Additionally, the residual stresses in the finished rectangular and square steel tubes were not included in the FE model, considering that the impact of them was significantly reduced after filling concrete into the space between the outer and inner steel tubes [14, 28].

The concrete damaged plasticity (CDP) model in ABAQUS [23], which defines the failure of concrete as compressive crushing and tensile cracking, shows good convergence. Therefore, it was chosen to model the complicated behaviour of sandwich concrete. The elastic properties, including the elastic modulus  $E_c$  and Poisson's ratio  $\mu_c$  were determined according to the provisions of ACI 318-19 [30] and CEB [31], respectively, i.e.  $E_c=4730\sqrt{f'_c}$  and  $\mu_c=0.2$ , where  $f'_c$  is the compressive cylinder strength. With reference to documents [14] and [15] as well as the test results in this study, it is assumed that the inner tubes can always reliably restrain the sandwich concrete before fracturing

of the bottom flange of the outer tube, which means that the behaviour of the sandwich concrete is similar to that of the concrete core in the rectangular CFST. Therefore, the compressive  $\sigma_c - \varepsilon_c$  relationship, which is suitable for the FE simulation of rectangular DCFSSST short columns [14], was selected for the sandwich concrete in the rectangular DCFSSST beams, and the detailed formulae are expressed as:

$$\sigma_c/f'_c = \begin{cases} 2(\varepsilon_c/\varepsilon_{cp}) - (\varepsilon_c/\varepsilon_{cp})^2 & (\varepsilon_c/\varepsilon_{cp} \leq 1) \\ \frac{\varepsilon_c/\varepsilon_{cp}}{a_1 \cdot (\varepsilon_c/\varepsilon_{cp} - 1) + \varepsilon_c/\varepsilon_{cp}} & (\varepsilon_c/\varepsilon_{cp} > 1) \end{cases} \quad (7)$$

where,  $\varepsilon_{cp} = (12.5f'_c + 800\xi^{0.2} + 1300) \times 10^{-6}$ ,  $\xi (= \alpha_n \cdot f_{yo}/f_{ck})$  is the nominal confinement factor,  $f_{ck}$  is the characteristic compressive strength of concrete [15],  $a_1 = (f'_c)^{0.1}/(1.2\sqrt{1 + \xi})$ , and  $k = 1.5(\varepsilon_{cp}/\varepsilon_c) + 1.6$ .

Moreover, the formula presented in reference [32] was employed to calculate the compression damage factor of sandwich concrete. Simultaneously, the stress-fracture energy relationship in ABAQUS [23] was used to specify tension-stiffening behaviour of sandwich concrete, and the failure stress and the fracture energy were respectively taken as  $0.1f'_c$  and 100 N/m [5, 31]. The plasticity parameters for the CDP model were determined by referring to the recommended values of the software package [23] and further corrected by the test results, as listed in Table 3.

The 4-node general-purpose shell elements with full integration (S4) suitable for large-strain analysis were chosen to simulate all the steel tubes, and the Simpson's rule with 9 integral points in direction of wall thickness was specified to meet the calculation accuracy. The 8-node three-dimensional solid elements C3D8R with reduced integration were selected to model the sandwich concrete, as they are appropriate for treating large strains with geometric nonlinearity and possible serious mesh distortion. The structured meshing strategy included in the software package [23] was employed, and the corner portions of all steel tubes were subdivided to ensure the convergence and accuracy. In order to accurately capture the fracture moment and post-fracture damage evolution of the steel tube, the element encryption was set within two quarter points of the rectangular DCFSSST beam specimens, and the element was deleted once it met the fracture criteria. Fig. 9 exhibits the

311 meshing for the FE model of the rectangular DCFSSST beams.

3112 The interaction between various components of the rectangular DCFSSST beams, including outer  
2  
313 and inner steel tubes as well as sandwich concrete, was simulated by defining the contact pairs. For  
4  
5  
314 the interface between the outer and inner steel tubes and sandwich concrete, the normal direction was  
7  
315 simulated by the ‘hard contact’, and the tangent directions were modelled by the ‘Coulomb friction’  
9  
10  
316 with friction coefficient equal to 0.6 [14], while setting both the inner wall of outer RHS and the outer  
12  
1317 wall of inner tubes as the master surface and the surface of sandwich concrete in contact with the  
14  
15  
318 above walls as the slave surface. Moreover, the interface between sandwich concrete and two  
17  
1319 endplates was also simulated by the ‘hard contact’, and the interface between the outer and inner steel  
19  
20  
320 tubes and the two endplates was defined as the ‘shell-to-solid coupling’.

23321 The boundary conditions for the FE model of the rectangular DCFSSST beams, shown in Fig. 9,  
24  
25  
322 have good agreement with those of the specimens tested within this study and literature references  
26  
27  
2323 [15-17]. Four reference points, RPs, were defined in ABAQUS such that they are located at the  
29  
3024 midpoint of the section width and they were set at the two loading positions and support positions  
31  
32  
3325 and each RP was coupled with the outer surface of outer tube at the corresponding area. The length  
34  
3526 of coupling area was set to be  $0.8B_o$  based on the comprehensive consideration of convergence,  
36  
37  
3327 accuracy and computational efficiency. For the RP corresponding to the fixed support, three  
39  
4028 translational degrees of freedom ( $U_x$ ,  $U_y$  and  $U_z$ ) and two rotational degrees of freedom ( $U_{r_y}$  and  
41  
42  
3329  $U_{r_z}$ ) were constrained, and for the RP corresponding to the rolling support, two translational degrees  
44  
4330 of freedom ( $U_x$  and  $U_y$ ) and two rotational degrees of freedom ( $U_{r_y}$  and  $U_{r_z}$ ) were constrained.  
46  
4731 The loading was carried out by imposing a displacement of 100 mm along the negative Y-axis on the  
48  
49  
5032 two quarter points in the span of the composite beam.

5323 In addition, the impact of initial geometric defects (IGDs) on the flexural performance of DCFSSST  
53  
54  
5334 beams was analyzed based on the FE model. The buckling eigenmode of outer and inner tubes in the  
56  
5735 composite beam was treated as the IGDs in the first analysis step, and the amplitude was equal to 0.1  
58  
59  
336 times the tube wall thickness [33]. Fig. 10 shows the impact of the initial geometric defects (IGDs)

on the flexural behaviour of the rectangular DCFSSST beam specimens and as seen in the figure, the FE simulation results with and without IGDs are close to each other and generally agree well with the measured results.

### 3.2. Validation of the FE model

Fig. 3(b) illustrates the simulated failure modes of rectangular DCFSSST beam specimens in this study. Comparison in Fig. 3 indicates that the results predicted by the FE model are located mainly within two quarter points of the span and they include multiple local bulges on the top flange and part of side walls of the outer tube and fracture of the bottom flange of the outer steel section, shown in Fig. 3(b1). Sandwich concrete is crushed at the site of local bulges of the outer tube and cracked within its lower part, as shown in Fig. 3(b2) and the global deflections of the inner tubes in Fig. 3(b3) generally agree well with the observations from the tests. The difference between the simulated and measured failure area in the specimens is mainly due to the fact that, the FE models cannot reasonably mimic the influence of the following factors: 1) the sizes and flatness of the specimens differ from the design considerations, 2) there are manufacture defects in the materials of the specimens, 3) the loading devices in the testing set-up have the unavoidable minor position deviation.

Fig. 11 presents the curves of  $M - u_m$  behaviour such that those labelled with letter ‘M’ indicate the measured ones and those labelled with letter ‘P’ the predicted ones. The available test results from this study and the ones from references [15-17] are generally in good agreement with the FE-predictions, except that the plastic hardening phase of the former is slightly higher, and the fracture moment and process of the former show a certain difference. This may be due to the deviation between the material properties from the standard tests and the real properties of the tubes and sandwich concrete in the specimens, and in the plastic phase the rolling support between the spreader beam and the specimen gradually move inward due to the increase of displacement, resulting in additional bending moments in the specimen, whilst in the FE model, the initial position of the rolling support is simplified to a fixed loading point. The predicted  $M - \varepsilon$  diagrams are compared with the measured data in Fig. 12. As can be seen from these figures, the development trend of the simulated



$M - \varepsilon$  curves generally fits well with that of the measured results, and the agreement between them is good in elastic and elastic-plastic phase, but the plastic phases of the curves are deviated. Moreover, the simulated and measured  $M - \varepsilon_T$  curves of the inner steel CHSs include obvious differences, possibly due to the slight deviation in the positions of the attached transverse strain gauges. Fig. 13 demonstrates the typical distributions of  $\varepsilon_L$  in the mid-span section on account of predicted and measured data. It is shown that, with the increase of  $m$ , the predicted distribution of  $\varepsilon_L$  and variation amplitude of cross-sectional neutral axis generally accord with the measured results when  $m \leq 0.9$ . However, for the results with  $m = 1.0$ , the discrepancy between the predicted and measured distribution becomes more evident. This may be caused by the subtle difference between the simulated and observed cracking characteristics of the concrete together with local bulge pattern of outer tube walls.

Fig. 14 presents a comparison between the simulated flexural capacity  $M_{u,fe}$  and the measured flexural capacity  $M_{u,e}$  within this study and references [15-17] and overall  $M_{u,fe}$  is close to  $M_{u,e}$  with the discrepancy limited to 10%. The mean value and Cov of  $M_{u,fe}/M_{u,e}$  are 0.976 and 0.039, verifying that the FE model is capable of predicting well the flexural capacity of the rectangular DCFSSST and CFDST beams.

### 3.3. Further numerical study

The FE model is further used to undertake numerical analysis of rectangular DCFSSST beams, and the simulation results indicate that the strength properties ( $f_{yo}$ ,  $f_{yi}$  and  $f'$ ) and  $d_i/t_i$  have very limited influence on the stress/strain distribution characteristics, while merely affecting the specific values. Therefore, the effect of key parameters, including  $\alpha_n$ ,  $\phi$ ,  $e_0$  and depth-to-breadth ratio of outer tube ( $\eta$ ), on the response of rectangular DCFSSST beams is numerically studied. The parameters for the benchmark are as follows:  $D_o=600$  mm,  $L/D_o=8.0$ ,  $\eta=2.0$ ,  $\alpha_n=0.10$ ,  $\phi=0.5$ ,  $e_0=0.5$ ,  $f'=50$  MPa,  $f_{yo}=f_{yi}=355$  MPa and  $d_i/t_i=40$  (SHS) or 60 (CHS). It should be noted that, while changing  $\eta$ , the section circumference of outer steel RHS is kept fixed.

Fig. 15 displays the influence of the key parameters on the stresses of the sandwich concrete in the

mid-span section at the moment of attaining the flexural capacity  $M_u$  and ‘S33’ represents the normal stress along the direction of the span indicated in Fig. 9, and the dashed line indicates the location of the neutral axis. Most of the sandwich concrete is stressed in tension with  $S_{33} > 0$  and the tensile stresses increase with the decrease of  $\alpha_n$ ,  $\phi$  and  $\eta$  and increase of  $e_0$ . The depth of the compressed section decreases with the increase of  $\alpha_n$  and  $\phi$  and remains almost unchanged with the variation of  $e_0$ , whereas  $\eta$  has no evident effect on the location of the neutral axis. Moreover, the stress distribution characteristics and maximum compressive stress of sandwich concrete change with the change of key parameters. In general, the maximum compressive stress appears at two top corners where sandwich concrete contacts with the outer tube, and under certain parameter conditions (e.g.  $\alpha_n=0.16$ ,  $\phi = 0.75$  or  $e_0=0.6$ ) the maximum compressive stress simultaneously arises at two top corners where sandwich concrete contacts with the upper inner tube. However, as the change of key parameters leads to the variation in the area and cross-section characteristics of the sandwich concrete in compression, its maximum stress does not indicate any consistent varying characteristics while the values of the parameters are increased or decreased.

The effects of  $\phi$  and  $e_0$  on the von Mises stress in the inner SHSs are demonstrated in Fig. 16 at the moment of reaching  $M_u$ , and the impact of other parameters have similar variation features. It is seen that within the centre-most quarters of the span the von Mises stress in the whole section of the lower tube exceeds  $f_{yi}$  in the tensile region of the sandwich concrete, but in most of the cases only the von Mises stress of the top flange and part of the sidewalls in the upper tube is greater than  $f_{yi}$ . For certain cases, e.g. with  $\phi=0.25$ , the von Mises stress of the upper tube remains less than  $f_{yi}$ , indicating that whole section of the lower tube has yielded while only partial or no yielding has occurred in the upper tube. The variation of parameters mainly determines the distribution characteristics of the von Mises stress of the upper tube. In general, when there is a yield area in the upper tube, the gradient of the von Mises stress between the top and bottom flange increases with the increase of  $\phi$  and the decrease of  $e_0$ .

Fig. 17 shows the influence of the key parameters on the interaction stress  $p$  in typical points of

the mid-span section. For a rectangular DCFST beam,  $p$  in the corner point 1 is higher than those in the other three points where the top flange of the outer tube is in contact with the sandwich concrete, and it decreases gradually after reaching the maximum value as the local bulge in the top flange extends to its corner. In the later phase of loading, stress  $p$  of the corner point 4 exceeds that of point 1. Stress  $p$  of the corner point 2 is close to that of point 4 in the early phase of loading but the difference in them increases gradually as  $u_m$  improves. Stress  $p$  of the corner point 3 is generally very small and the four parameters have no regular influence on the  $p - u_m$  relationship of points 1, 2 and 4, since the location of the neutral axis of the cross-section varies continuously with the development of cracking in the sandwich concrete and local bulge in the walls of the tube.

#### 4. Simplified calculation of flexural capacity

Fig. 18 presents the results for the flexural capacity  $M_u$  in the rectangular DCFST beams calculated using the FE model under various parametric conditions and as compared with the composite beams having inner CHSs, higher values of  $M_u$  exist for the beams with inner SHSs. With the improvement of parameters  $\alpha_n$ ,  $\phi$ ,  $e_0$ ,  $f_{y0}$ ,  $f_{yi}$ , and  $f'_c$  and reduction of  $d_i/t_i$  the flexural capacity increases and the variation of  $\alpha_n$  and  $f_{y0}$  has a greater impact on  $M_u$ .

By referring to the method for the rectangular CFDST beams in [15] and taking the above numerical results into consideration, the flexural capacity of rectangular DCFST beams,  $M_u$ , can be calculated as the compound sum of the capacity values for the outer steel RHS together with the sandwich concrete,  $M_{osc,u}$  and for the inner steel tubes,  $M_{i,u}$ :

$$M_u = M_{osc,u} + M_{i,u} \quad (8)$$

For the compound section of outer steel RHS together with sandwich concrete, coefficient  $\gamma_{m,o}$  for the cross-sectional moment capacity is defined as:

$$\gamma_{m,o} = \frac{M_{osc,u}}{W_{scm} \cdot f_{oscy}} \quad (9-1)$$

$$W_{scm} = \begin{cases} \frac{1}{6} B_o \cdot D_o^2 - \left( \frac{d_i^4}{16} + \frac{d_i^2 \cdot d_e^2}{4} \right) / D_o & \text{(with inner SHSs)} \\ \frac{1}{6} B_o \cdot D_o^2 - \pi \left( \frac{d_i^4}{16} + \frac{d_i^2 \cdot d_e^2}{4} \right) / D_o & \text{(with inner CHSs)} \end{cases} \quad (9-2)$$

$$f_{oscy} = C_1 \cdot \phi^2 \cdot f_{y0} + C_2 \cdot (1.18 + 0.85\xi) \cdot f_{ck} \quad (9-3)$$

where,  $W_{scm}$  and  $f_{oscy}$  are the compound elastic section modulus and the characteristic value of compound axial compressive strength [15]; and the parameters  $C_1$  and  $C_2$  equal to  $\alpha_1/(1 + \alpha_1)$  and  $(1 + \alpha_n)/(1 + \alpha_1)$  respectively, and  $\alpha_1 = A_{so}/A_c$ ,  $A_c$  is the cross-sectional area of sandwich concrete.

The results in Fig. 16 indicate that when reaching  $M_u$ , yielding in the whole section and its parts generally appear in the lower and upper inner tubes of the DCFSSST beams, respectively, and accordingly the use of plastic section modulus,  $W_{psi}$ , is more suitable for calculating  $M_{i,u}$ . Coefficient  $\gamma_{m,i}$  for the cross-sectional moment capacity of the inner steel tubes is defined as:

$$\gamma_{m,i} = \frac{M_{i,u}}{W_{psi} \cdot f_{yi}} \quad (10-1)$$

$$W_{psi} = \begin{cases} \frac{\pi d_e}{4} \cdot [d_i^2 - d_i^2 - 2t_i] & \text{(with inner SHSs)} \\ d_e \cdot [d_i^2 - (d_i - 2t_i)] & \text{(with inner CHSs)} \end{cases} \quad (10-2)$$

The simulation results indicate that, the impact of  $\alpha_n$ ,  $f_{yo}$  and  $f'_c$  on  $\gamma_{m,o}$  and  $\gamma_{m,i}$  can be unified into the parameter  $\xi$ , which is determined by the above three parameters. The influence of the key parameters on the relationship between the coefficients  $\gamma_{m,o}$  and  $\gamma_{m,i}$  for the cross-sectional moment capacity and the longitudinal strain  $\varepsilon_{L,bf}$  of the bottom flange in the outer steel RHS is presented in Fig. 19 and the other parameters have only a moderate effect. In general, only the type of the inner tube has some influence on the form of the later phase in the  $\gamma_{m,o} - \varepsilon_{L,bf}$  diagram, but in terms of  $M_u$  corresponding to  $\varepsilon_{L,bf} = 0.01$ , the difference in  $\gamma_{m,o}$  and  $\gamma_{m,i}$  of rectangular DCFSSST beams with different types of inner tubes is generally less than 5% and therefore this influence is ignored. In addition,  $\gamma_{m,o}$  and  $\gamma_{m,i}$  improve with the increase of  $\xi$ ,  $\phi$  and  $e_0$ . Using the regression analysis for a suitable amount of the simulation data, the expressions for  $\gamma_{m,o}$  and  $\gamma_{m,i}$  are presented as:

$$\gamma_{m,o} = [1.27 + 0.35\ln(\xi)] \cdot (0.3\phi + 0.85) \cdot (0.62e_0 + 0.69) \quad (11)$$

$$\gamma_{m,i} = [0.85 + 0.12\ln(\xi)] \cdot (0.5\phi + 0.5) \cdot (e_0 + 0.85) \quad (12)$$

Fig. 20 presents the comparison between the simplified and simulated values of the coefficients, and it is shown that both  $\gamma_{m,o}$  and  $\gamma_{m,i}$  can be predicted well using the simplified formulae. The

final formula for the flexural capacity of rectangular DCFSSST beams is produced by inserting all the relevant parameters into Eq. (8). In Fig. 21 the values of simplified formulae for  $M_{u,s}$  are compared with a considerable number of results from the FE simulations,  $M_{u,fe}$ , and the actual models  $M_{u,e}$  based on the measured data. The difference between the simplified models and the simulated and measured results is generally less than 10%. The statistical outcome is that the mean and Cov of  $M_{u,s}/M_{u,fe}$  are 1.045 and 0.040, respectively, and for  $M_{u,s}/M_{u,e}$  they are 0.911 and 0.050, respectively, showing that the simplified formulae are capable of predicting accurately the flexural capacity of rectangular DCFSSST beams. The scope of application for the simplified equations is:  $\eta=1.2$  to  $2.0$ ,  $\alpha_n=0.04$  to  $0.16$ ,  $\phi=0.25$  to  $0.75$ ,  $e_0=0.4$  to  $0.6$ ,  $f_{yo}=f_{yi}=235$  MPa to  $460$  MPa,  $f'_c=31.9$  MPa to  $65$  MPa, and  $d_i/t_i=20$  to  $60$  for SHS or  $30$  to  $90$  for CHS.

## 5. Conclusions

The main conclusions from the experimental and numerical investigation on the flexural behaviour of rectangular DCFSSST beams reported in this paper are summarized as:

(1) The investigated beam specimens exhibit good deformability and their ultimate mid-span displacement is between 6% and 9% of the effective span length. The failure patterns include mainly multiple local bulge regions on the top flange of the outer tube, global deformation of the inner tubes and crushing of concrete at the evident sites of local bulge and nearly uniform cracks that extend to approx. 2/3 of the section depth in the sandwich concrete.

(2) Three successive phases in the  $M - u_m$  diagrams are classified as approximately elastic, elastic-plastic and plastic strengthening one before the fracture of the bottom flange in the outer tube. The displacement distribution of the beam specimens fits well with the half-sine wave form up to reaching the flexural capacity.

(3) The cross-section form of the inner tubes has a limited effect on the behaviour, but  $\alpha_n$  influences significantly on the values of  $M_{ue}$  and  $K_{ie}$  in the rectangular DCFSSST specimens. In the ones with inner SHSs and  $\alpha_n$  equal to 0.110 and 0.142,  $M_{ue}$  is 1.206 and 1.510 times that with  $\alpha_n$  equal to 0.079, respectively, and  $K_{ie}$  is 1.112 and 1.409 times that with  $\alpha_n$  equal to 0.079, and for

the specimens with inner CHSs, the values equal to 1.130 and 1.556 are associated with  $M_{ue}$  and respectively the values equal to 1.132 and 1.494 are associated with  $K_{ie}$ . The flexural stiffness of the specimens calculated using the superposition principle accords generally well with the ones based on the measured results.

(4) The established FE model predicts well the flexural performance of rectangular DCFSSST beams, and the FE model can be further used to reveal the overall stress and strain states of each component in the rectangular DCFSSST beams. The simplified formulae for the flexural capacity of rectangular DCFSSST beams suggested based on the data from the parametric analyses agree well with the numerical and experimental results.

## Declaration of Competing Interest

The authors declare that they have no known competing financial interests or personal relationships that could have appeared to influence the work reported in this paper.

## Acknowledgement

The research work reported herein was supported by the National Natural Science Foundation of China (No. 51678105). The research funding is highly appreciated.

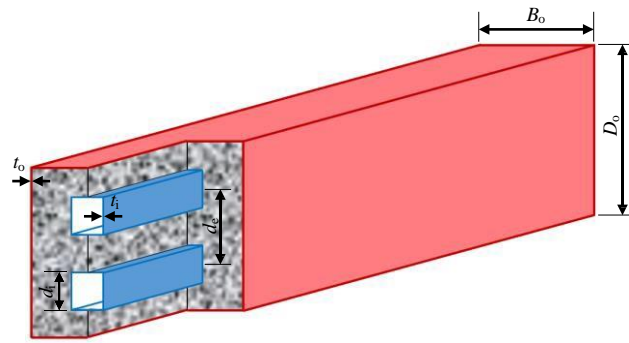
## References:

- [1] X.L. Zhao, R. Grzebieta, Strength and ductility of concrete filled double skin (SHS inner and SHS outer) tubes, *Thin-Walled Struct.* 40(2) (2002) 199-213.
- [2] L.H. Han, D. Lam, D.A. Nethercot, *Design Guide for Concrete-Filled Double Skin Steel Tubular Structures*, CRC Press, UK, 2018.
- [3] Y.F. Yang, C. Hou, Z. Wen, L.H. Han, Experimental behaviour of square CFST under local bearing forces, *Thin-Walled Struct.* 74 (2014) 166-183.
- [4] P. Ayough, N.H.R. Sulong, Z. Ibrahim, Analysis and review of concrete-filled double skin steel tubes under compression, *Thin-Walled Struct.* 148 (2020) 106495.
- [5] Y.F. Yang, X.M. Bie, F. Fu, Static performance of square CFDST chord to steel SHS brace T-joints, *J. Constr. Steel Res.* 183 (2021) 106726.
- [6] F. Zhou, W. Xu, Cyclic loading tests on concrete-filled double-skin (SHS outer and CHS inner) stainless steel tubular beam-columns, *Eng. Struct.* 127 (2016) 304-318.
- [7] J. Wang, W. Wang, L. Guo, Seismic tests and nonlinear model of beam-CFDST column joints with blind fasteners, *J. Building Eng.* 45 (2022) 103415.

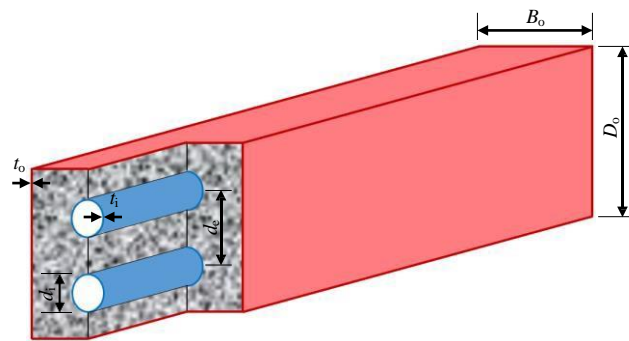
- [8] Y. Hu, J. Zhao, D. Zhang, H. Zhang, Cyclic tests of fully prefabricated concrete-filled double-skin steel tube/moment-resisting frames with beam-only-connected steel plate shear walls, *Thin-Walled Struct.* 146 (2020) 106272.
- [9] R. Wang, L.H. Han, X.L. Zhao, K.J.R. Rasmussen, Analytical behavior of concrete filled double steel tubular (CFDST) members under lateral impact, *Thin-Walled Struct.* 101 (2016) 129-140.
- [10] W. Li, Y.Z. Gu, L.H. Han, X.L. Zhao, Behaviour of grout-filled double-skin steel tubular T-joint subjected to low-velocity impact, *Thin-Walled Struct.* 144 (2019) 106270.
- [11] H. Lu, X.L. Zhao, L.H. Han, FE modelling and fire resistance design of concrete filled double skin tubular columns, *J. Constr. Steel Res.* 67(11) (2011) 1733-1748.
- [12] Y. Yao, H. Li, K. Tan, Theoretical and numerical analysis to concrete filled double skin steel tubular columns under fire conditions, *Thin-Walled Struct.* 98 (2016) 547-557.
- [13] A.L. Camargo, J.P.C. Rodrigues, R.H. Fakury, L. Laim, Fire resistance of axially and rotationally restrained concrete-filled double-skin and double-tube hollow steel columns, *J. Struct. Eng.* 145(11) (2019) 04019128.
- [14] Y.F. Yang, Y.Q. Zhang, F. Fu, Axial compressive behaviour of rectangular DCFSSST stub columns, *J. Constr. Steel Res.* 199 (2022) 107592.
- [15] Z. Tao, L.H. Han, Behaviour of concrete-filled double skin rectangular steel tubular beam-columns, *J. Constr. Steel Res.* 62(7) (2006) 631-646.
- [16] L.H. Han, Z. Tao, H. Huang, X. L. Zhao, Concrete-filled double skin (SHS outer and CHS inner) steel tubular beam-columns, *Thin-Walled Struct.* 42(9) (2004) 1329-1355.
- [17] W. Ashraf, M. Usman, S.H. Farooq, N. Ullah, S. Saleem, 2022. Flexural properties of concrete-filled, double-skin, square-hollow-section tubular beams, *Proc. Inst. Civil Eng.-Struct. Build.* 175(7) (2022) 577-589.
- [18] C.B. Ritchie, J.A. Packer, M.V. Seica, X.L. Zhao, Flexural behavior of concrete-filled double-skin tubes subject to blast loading, *J. Struct. Eng.* 144(7) (2018) 04018076.
- [19] X. Liu, H. Xu, X. Wang, B. Wang, L. Ma, Flexural behavior of concrete-filled double-skin steel tubular beams after subject to high temperature, *J. Constr. Steel Res.* 175 (2020) 106324.
- [20] Y.F. Yang, Y.Q. Zhang, F. Fu, Performance and design of RAC-filled steel RHS beams, *J. Build. Eng.* 46 (2022) 103734.
- [21] L.H. Han, Y.F. Yang, Z. Tao, Concrete-filled thin-walled steel SHS and RHS beam-columns subjected to cyclic loading, *Thin-Walled Struct.* 41(9) (2003) 801-833.
- [22] L.H. Han, H. Huang, X.L. Zhao, Analytical behaviour of concrete-filled double skin steel tubular (CFDST) beam-columns under cyclic loading, *Thin-Walled Struct.* 47(6-7) (2009) 668-680.
- [23] Simulia, ABAQUS 6.14 Analysis User's Manual, Dassault Systemes Simulia Corp., Providence, RI, USA, 2014.

- [24]N. Abdel-Rahman, K.S. Sivakumaran, Material properties models for analysis of cold-formed steel members, *J. Struct. Eng.* 123(9) (1997) 1135-1143.
- [25]M. Elchalakani, X.L. Zhao, R. Grzebieta, Tests on concrete filled double-skin (CHS outer and SHS inner) composite short columns under axial compression, *Thin-Walled Struct.* 40(5) (2002) 415-441.
- [26]H.L. Yu, D.Y. Jeong, Application of a stress triaxiality dependent fracture criterion in the finite element analysis of unnotched Charpy specimens, *Theor. Appl. Fract. Mech.* 54(1) (2010) 54-62.
- [27]T. Wierzbicki, Y. Bao, Y.W. Lee, Y. Bai, Calibration and evaluation of seven fracture models, *Int. J. Mech.Sci.*, 47(4-5) (2005) 719-743.
- [28]Z. Tao, Z.B. Wang, Q. Yu, Finite element modelling of concrete-filled steel stub columns under axial compression, *J. Constr. Steel Res.* 89 (2013) 121-131.
- [29]Y.F. Yang, F. Fu, X.M. Bie, X.H. Dai, Axial compressive behaviour of CFDST stub columns with large void ratio, *J. Constr. Steel Res.* 186 (2021) 106892.
- [30]ACI Committee 318, Building Code Requirements for Structural Concrete (ACI 318-19) and Commentary, American Concrete Institute, Detroit, USA, 2019.
- [31]CEB (Comité Euro-International du Béton), CEB-FIP Model Code 1990: Design Code, Thomas Telford, London, UK, 1993.
- [32]V. Birtel, P. Mark, Parameterised finite element modelling of RC beam shear failure, *Proceedings of the 19th Annual International ABAQUS Users' Conference*, Boston, USA, (2006) 95-108.
- [33]Z. Lai, A.H. Varma, L.G. Griffis, Analysis and design of noncompact and slender CFT beam-columns, *J. Struct. Eng.* 142(1) (2016) 04015097.



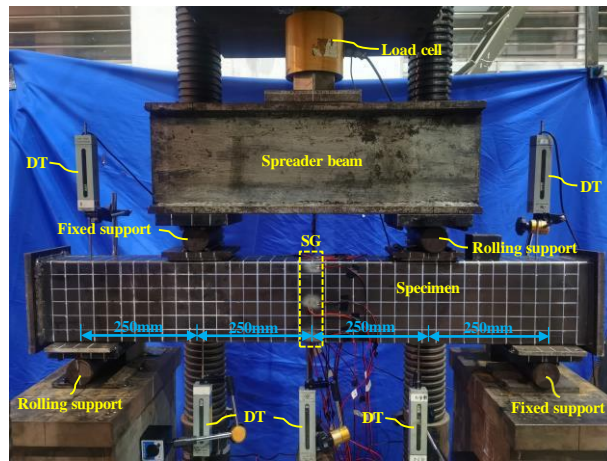
**Figures:**

(a) With inner SHSs

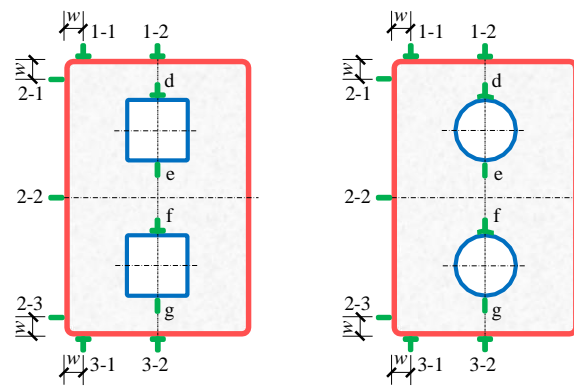


(b) With inner CHSs

**Fig. 1.** Configuration of the rectangular DCFSSST beams.

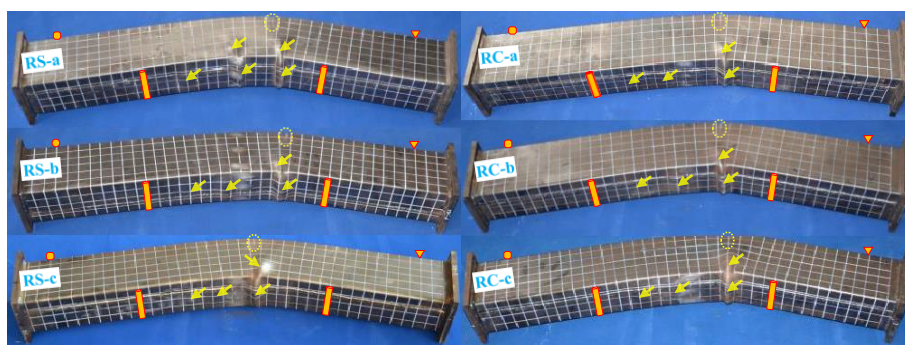


(a) General layout



(b) Layout of strain gauges ( $w=20$  mm)

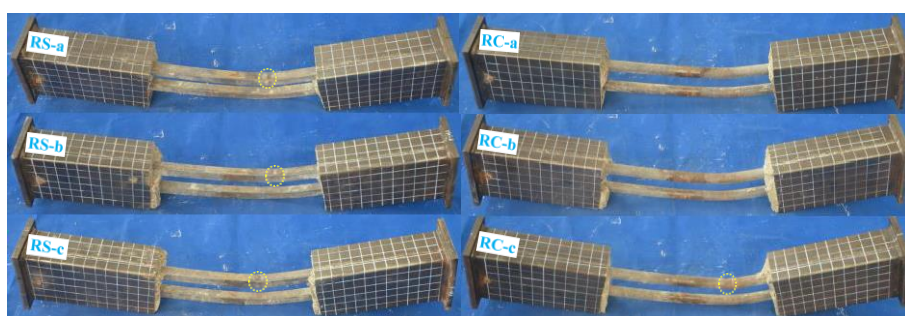
**Fig. 2.** Testing set-up.



(1) Overall appearance



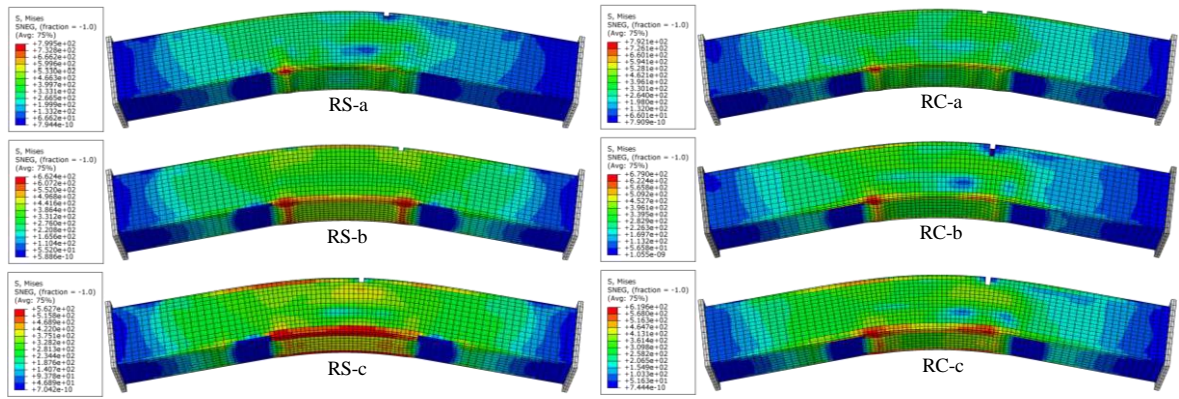
(2) Sandwich concrete



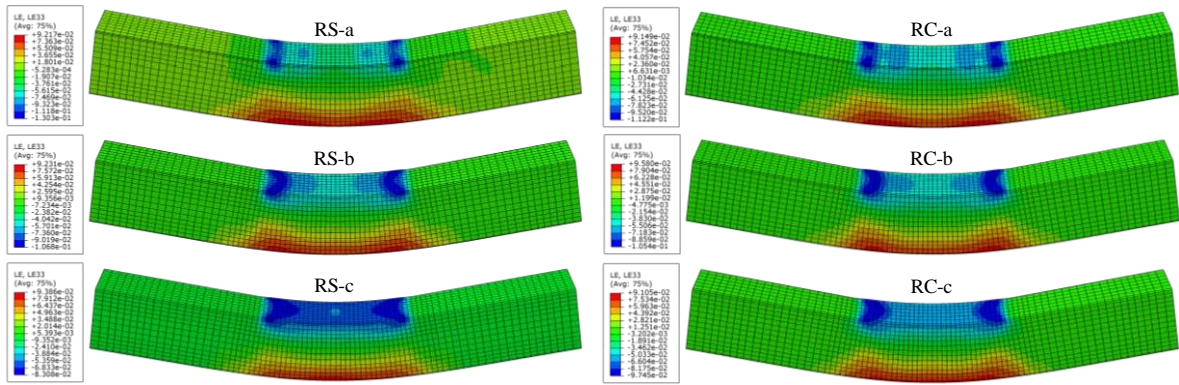
(3) Inner tubes

(a) Measured result

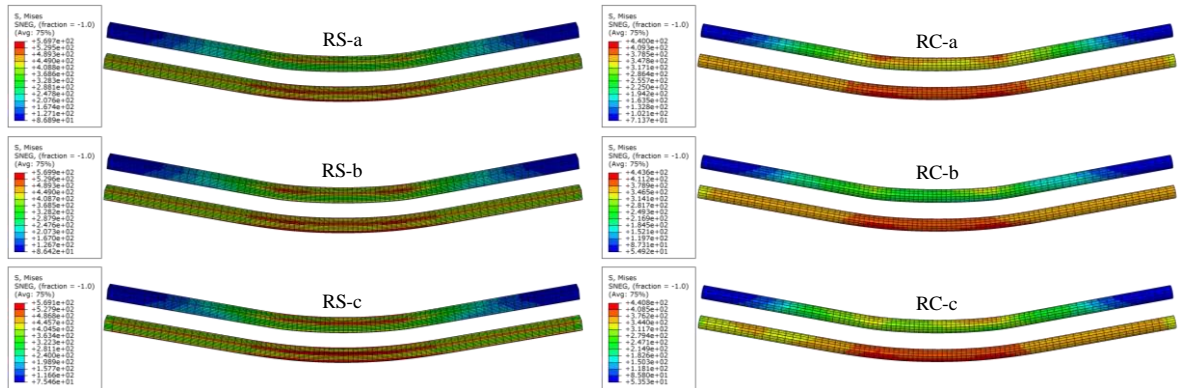
**Fig. 3.** (continued).



(1) Overall appearance



(2) Sandwich concrete



(3) Inner tubes

(b) Simulated result

**Fig. 3.** Failure modes of rectangular DCFST beam specimens.

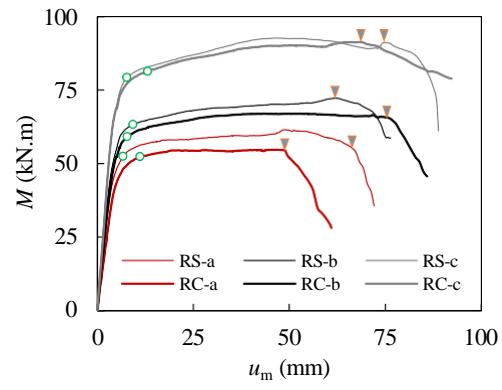
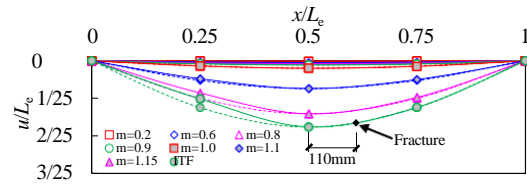
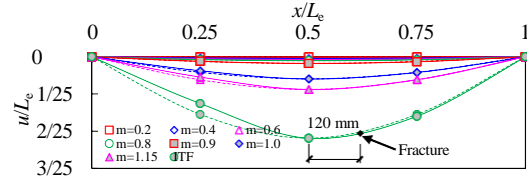


**Fig. 4.**  $M - u_m$  curves for the specimens according to the measurements.



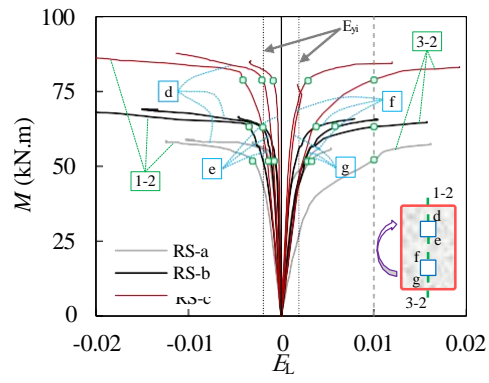
(a) RS-b



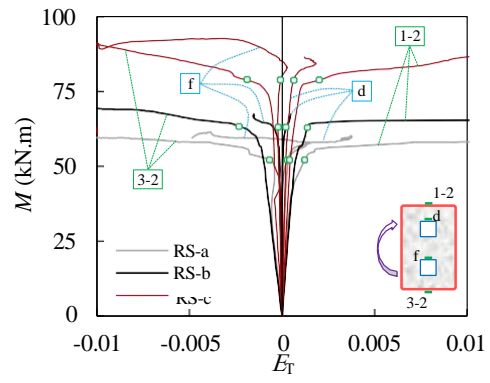
(b) RC-b

**Fig. 5.** Distribution of deflections along effective span of typical specimens.

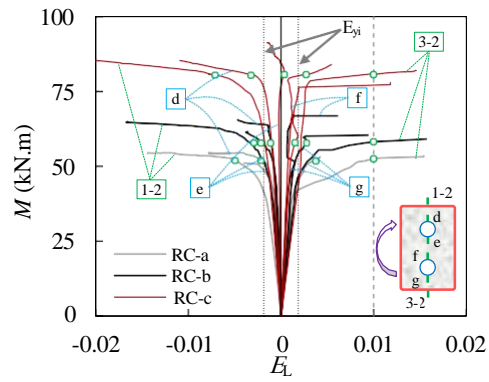




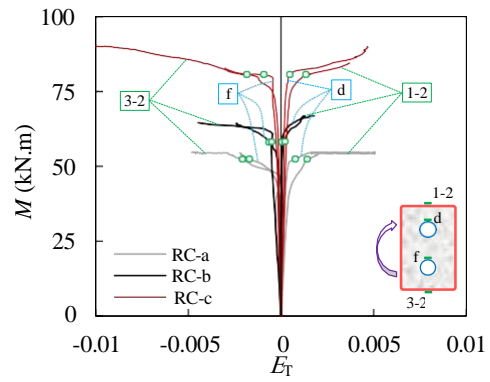
(a)  $\varepsilon_L$  of RS group specimens



(b)  $\varepsilon_T$  of RS group specimens

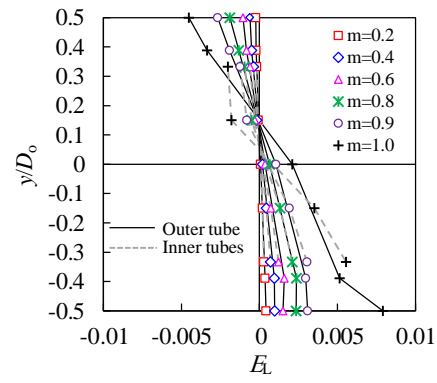


(c)  $\varepsilon_L$  of RC group specimens

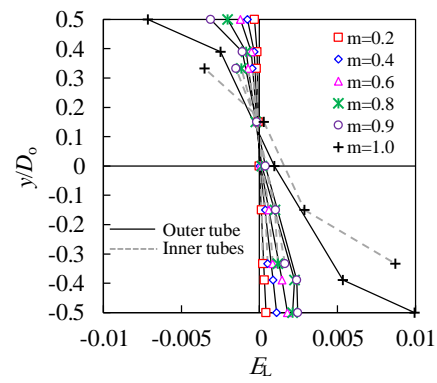


(d)  $\varepsilon_T$  of RC group specimens

**Fig. 6.** Relationships between  $\varepsilon_L$ ,  $\varepsilon_T$  and  $M$  according to the recorded data.



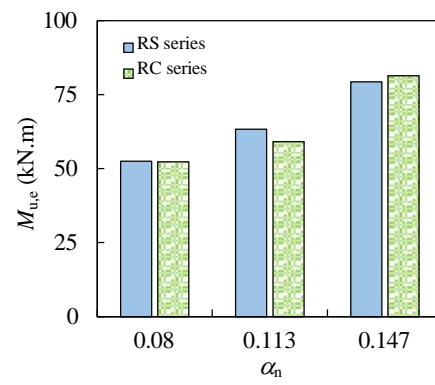
(a) RS-b



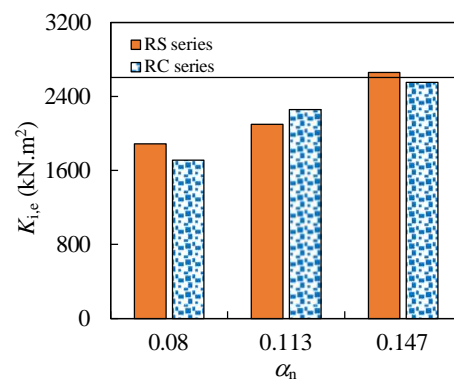
(b) RC-c

**Fig. 7.** Distribution of  $\epsilon_L$  in the mid-span section of typical specimens.





(a) Flexural capacity



(b) Flexural stiffness

**Fig. 8.** Effects of varying  $\alpha_n$  on the mechanical index in the specimens.

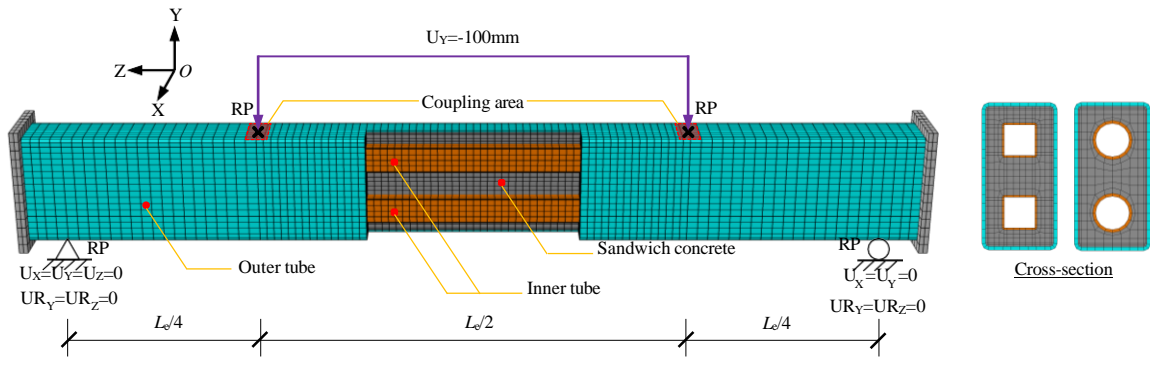


**Fig. 9.** Meshing and boundary conditions for the FE model of the rectangular DCFST beams.

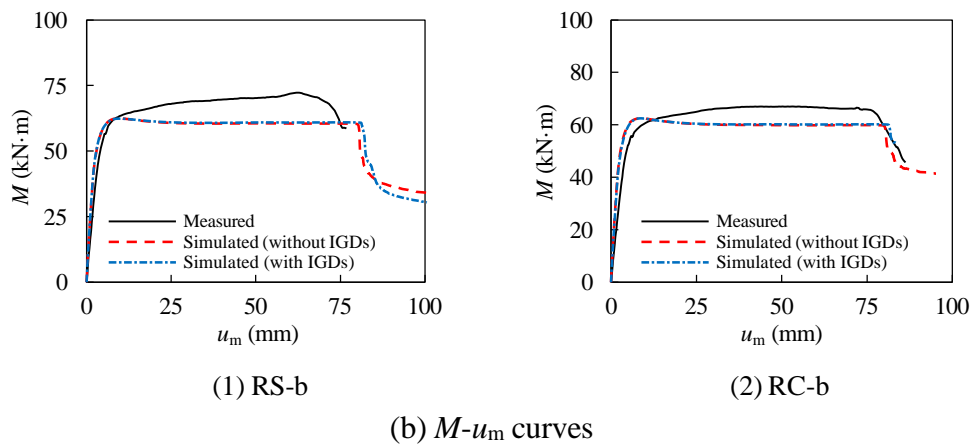
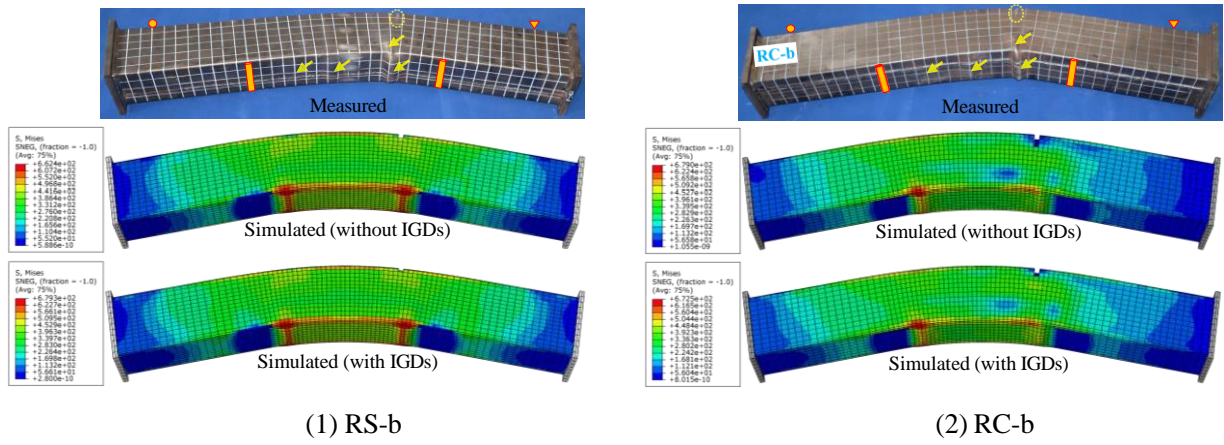


**Fig. 10.** Impact of the initial geometric defects (IGDs) on the flexural behaviour of the rectangular DCFSSST beam specimens.

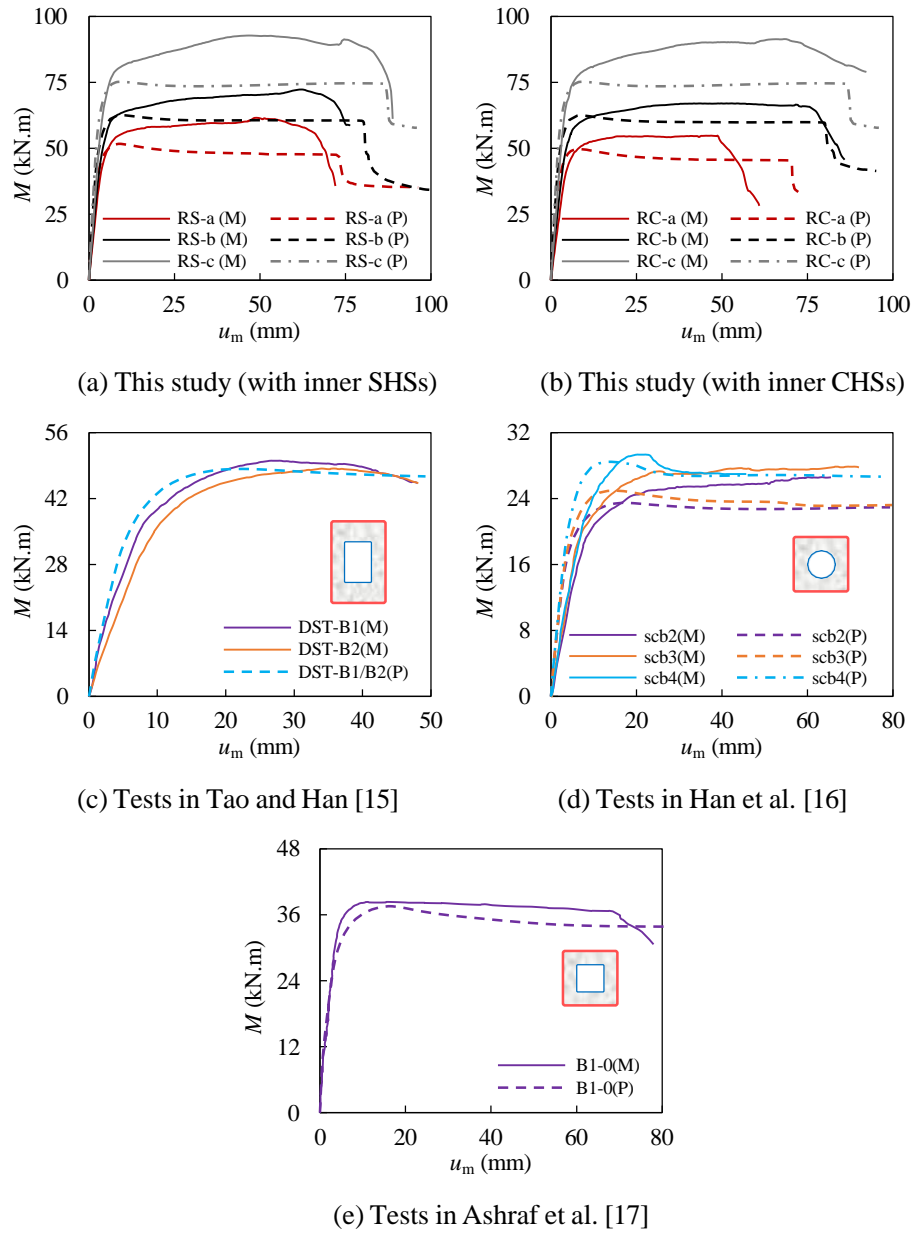


**Fig. 11.** Comparison between the predicted and measured  $M - u_m$  curves.

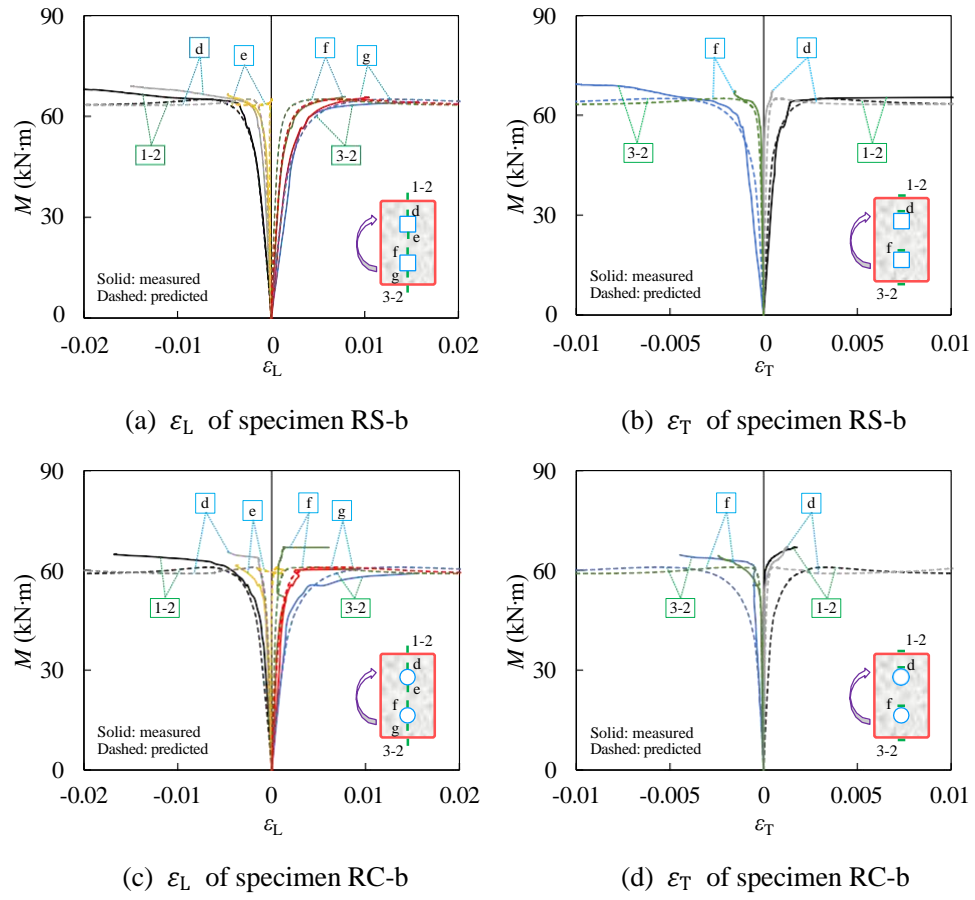
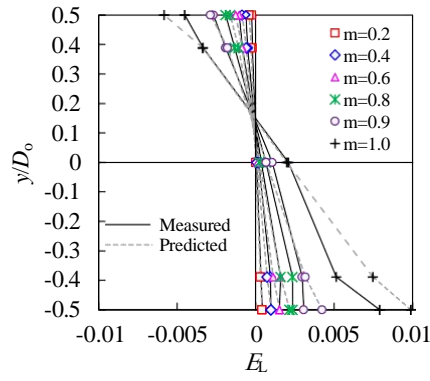
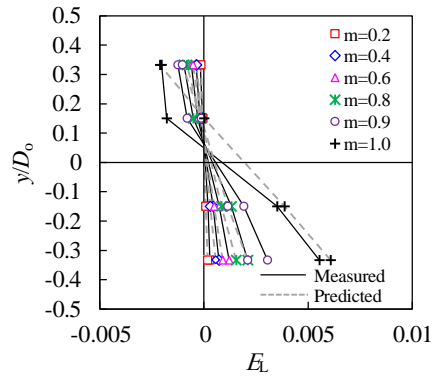


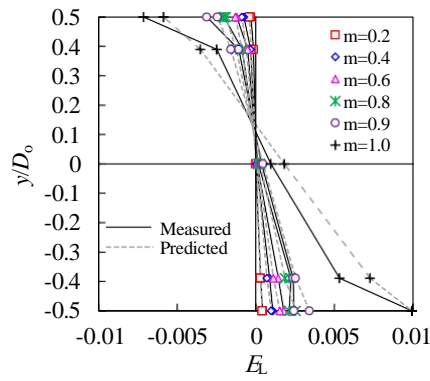
**Fig. 12.** Typical  $M - \varepsilon_L$  and  $M - \varepsilon_T$  diagrams according to predictions and measured data.



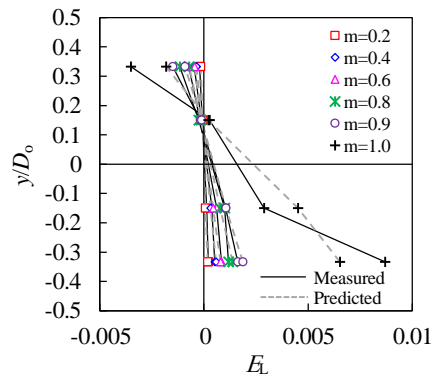
(a) Outer tube of specimen RS-b



(b) Inner tubes of specimen RS-b



(c) Outer tube of specimen RC-c



(b) Inner tubes of specimen RC-c

**Fig. 13.** Typical distributions of  $\epsilon_L$  in the mid-span section on account of predicted and measured data.

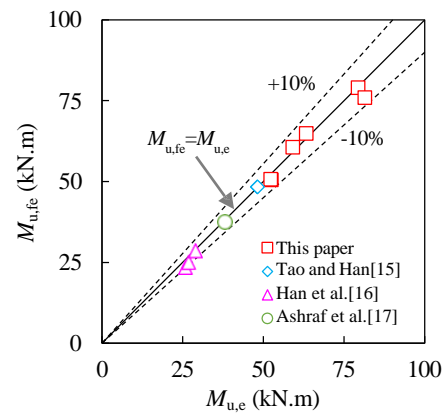


**Fig. 14.** Comparison of flexural capacities evaluated on account of predicted and measured data.

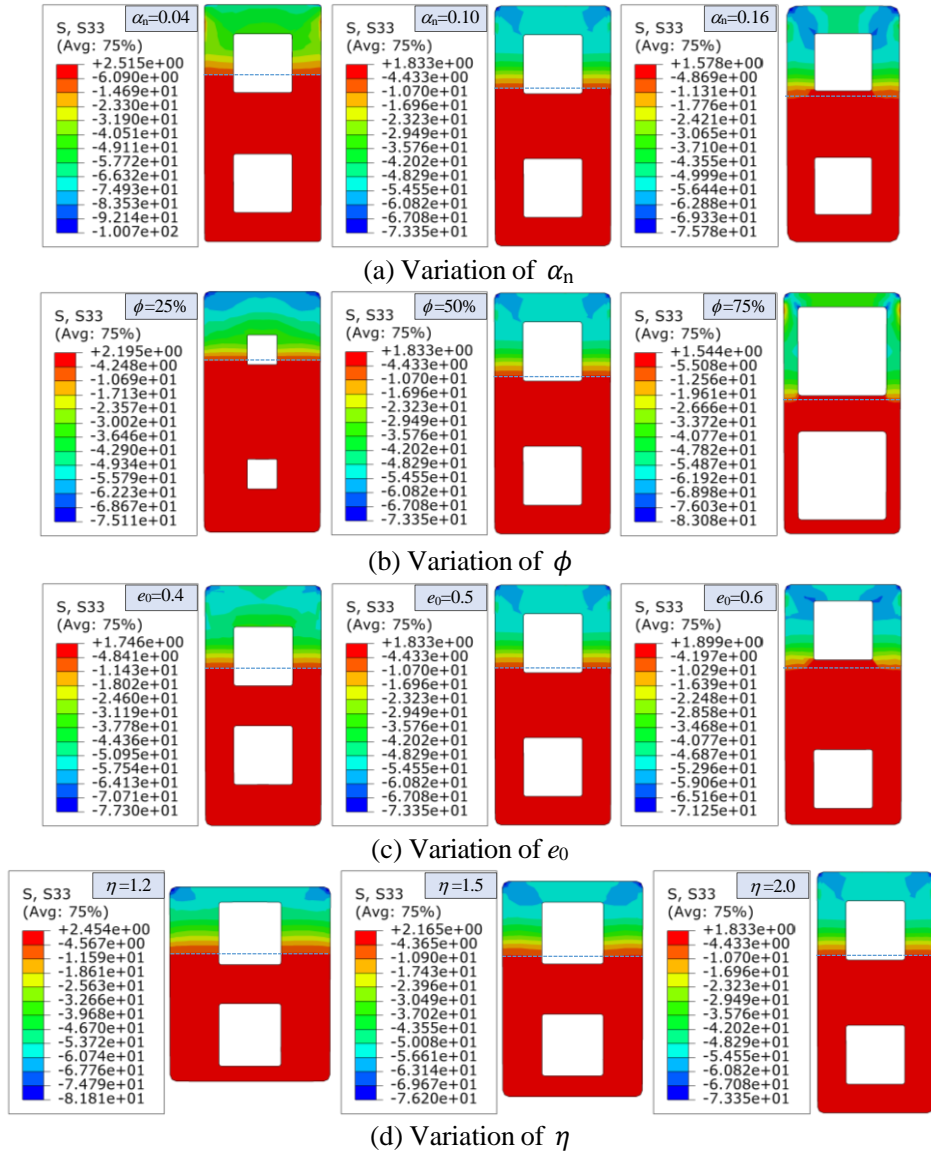
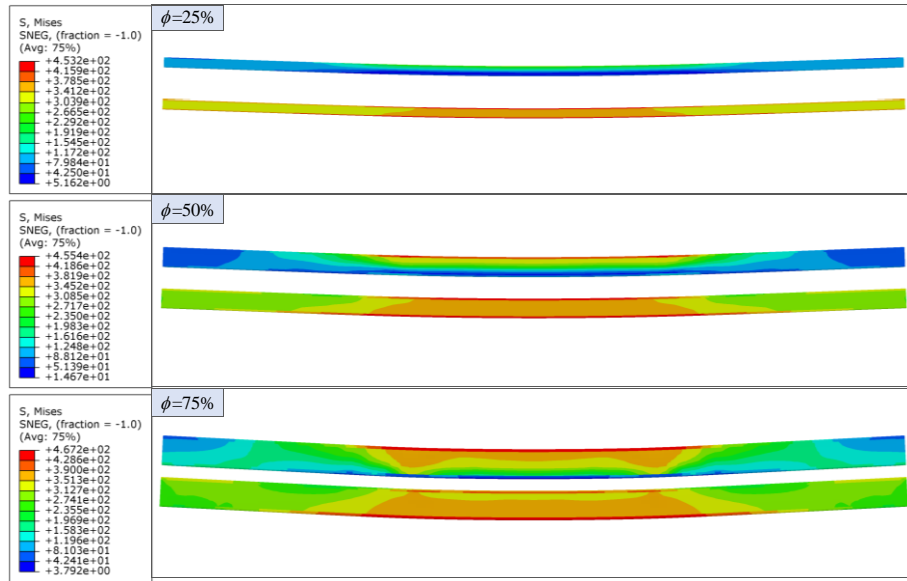
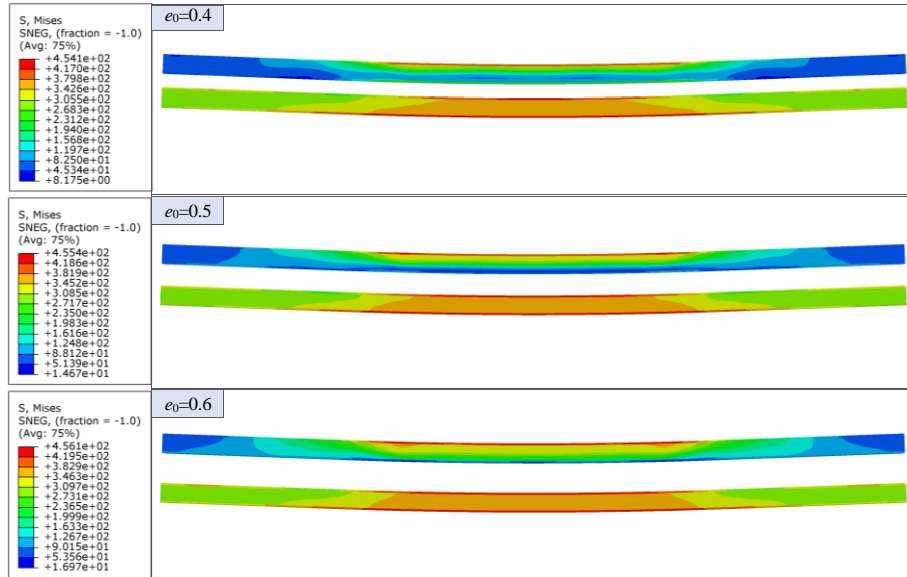


**Fig. 15.** Influence of the key parameters on the stresses of sandwich concrete in the mid-span section.



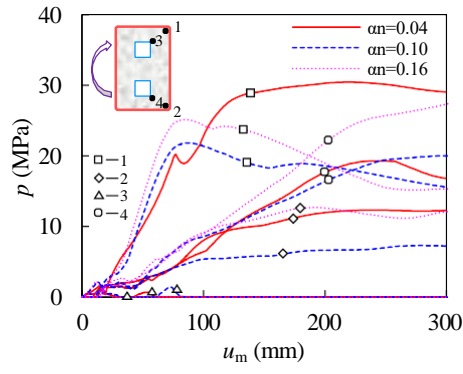


(a) Variation of  $\phi$

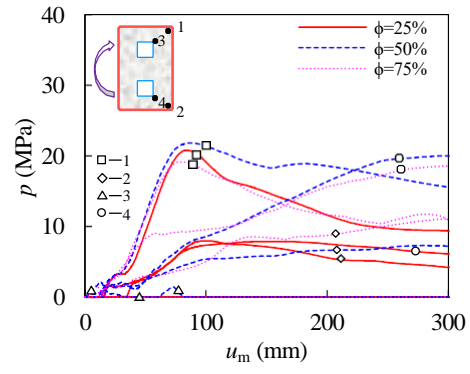


(b) Variation of  $e_0$

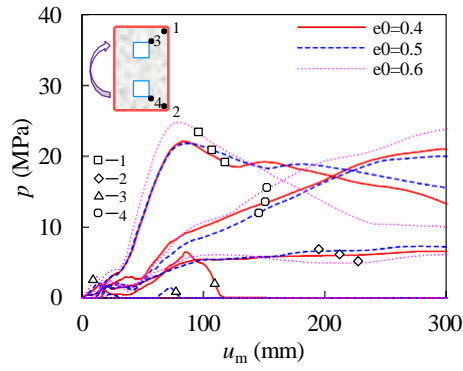
**Fig. 16.** Effects of  $\phi$  and  $e_0$  on the von Mises stresses in the inner SHSs.



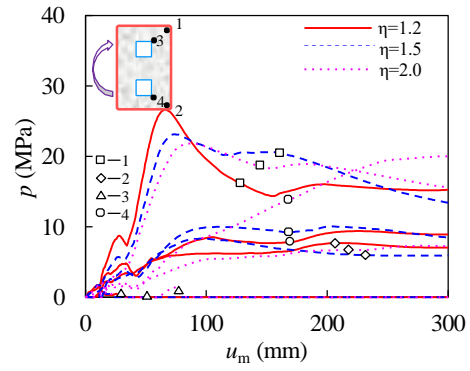
(a) Variation of  $\alpha_n$



(b) Variation of  $\phi$



(c) Variation of  $e_0$



(d) Variation of  $\eta$

**Fig. 17.** Influence of the key parameters on the interaction stress  $p$  in typical points of the mid-span section.

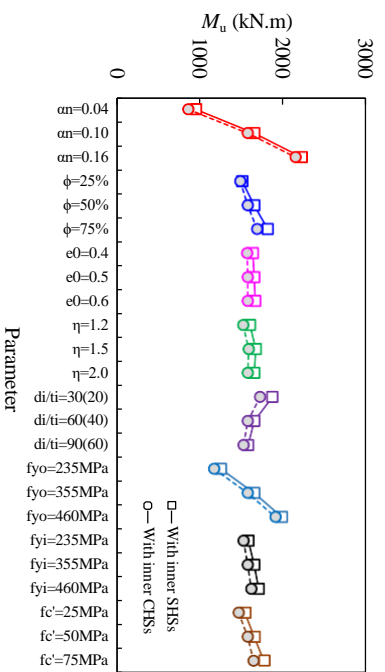
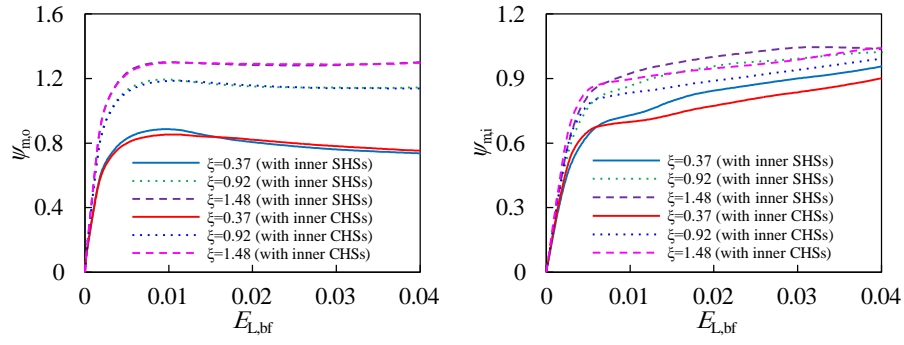
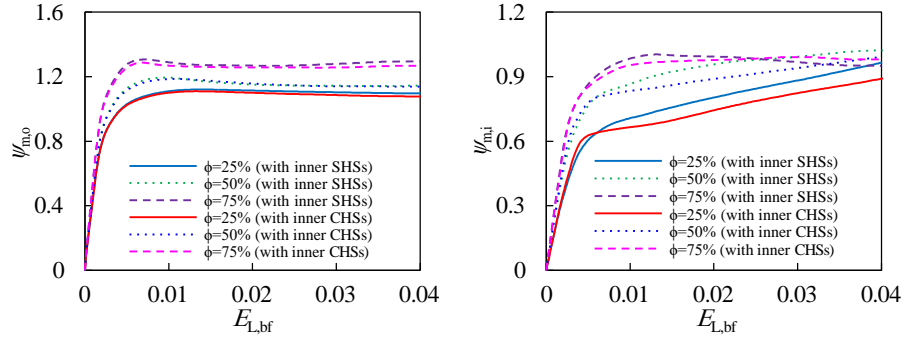


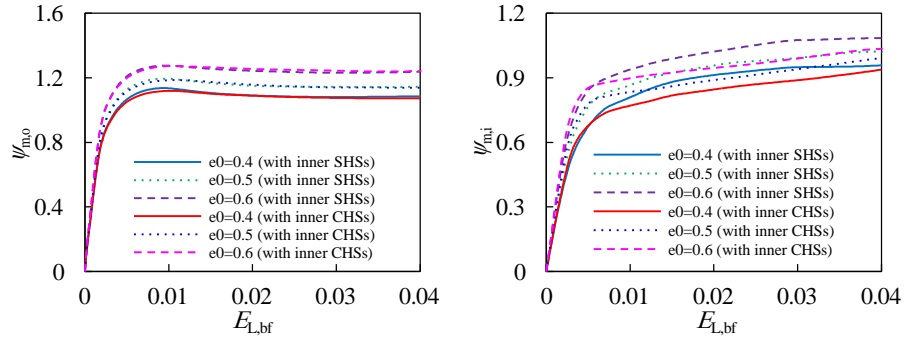
**Fig. 18.** Effect of key parameters on the values of  $M_u$  in rectangular DCFST beams.



(a) Confinement factor,  $\xi$



(b) Void ratio,  $\phi$



(c) Offset ratio of inner steel tube,  $e_0$

**Fig. 19.** Effect of key parameters on  $\gamma_{m,o}$  and  $\gamma_{m,i}$ .

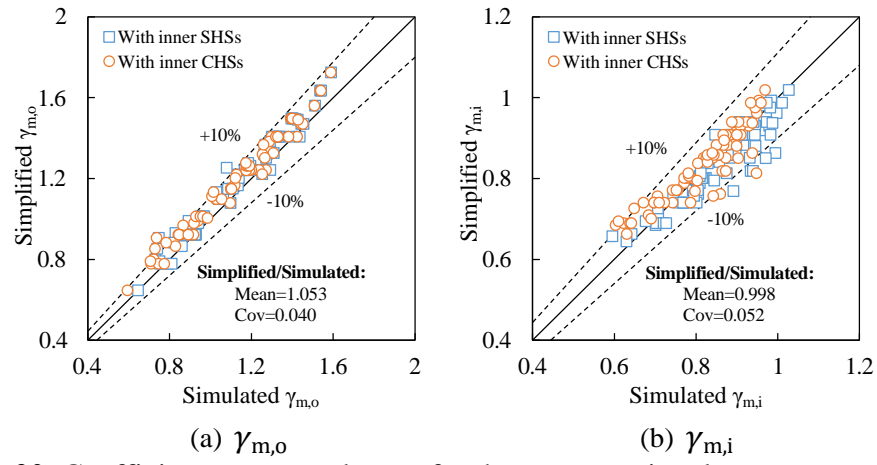


**Fig. 20.** Coefficients  $\gamma_{m,o}$  and  $\gamma_{m,i}$  for the cross-sectional moment capacity.

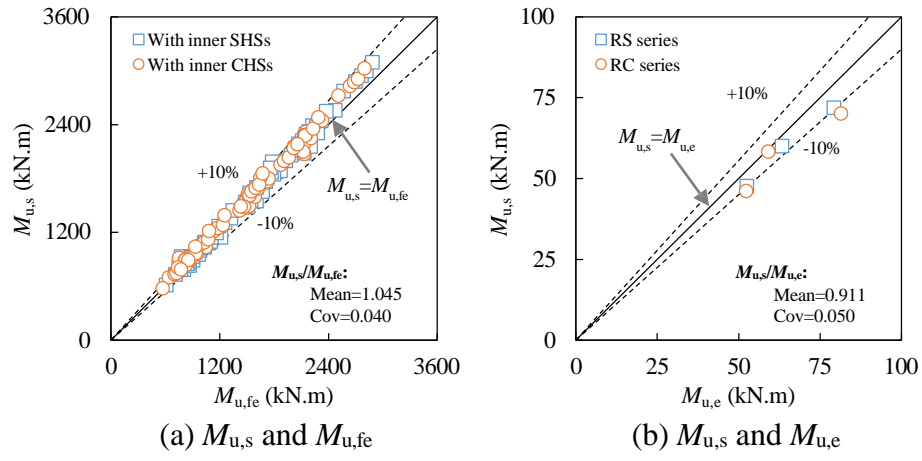


**Fig. 21.** Flexural capacities based on simplified equations, simulation data and measured data.

## **Tables:**

**Table 1.** Details of the specimens.

| No. | Label | $D_o \times B_o \times t_o$<br>(mm) | $d_i \times t_i$<br>(mm) | $\alpha_n$ | $\phi$ | $d_e$<br>(mm) | $e_0$ | $f_{yo}$<br>(MPa) | $f_{yi}$<br>(MPa) | $f_{cu}$<br>(MPa) | $M_{u,e}$<br>(kN·m) | $K_e$<br>(kN·m <sup>2</sup> ) |
|-----|-------|-------------------------------------|--------------------------|------------|--------|---------------|-------|-------------------|-------------------|-------------------|---------------------|-------------------------------|
| 1   | RS-a  | 180×120×2.68                        | 30×1.94                  | 0.079      | 30.0%  | 90            | 0.50  | 324.9             | 371.8             | 49.8              | 52.5                | 1888.4                        |
| 2   | RS-b  | 180×120×3.66                        | 30×1.94                  | 0.110      | 30.4%  | 90            | 0.50  | 333.7             | 371.8             | 49.8              | 63.3                | 2099.1                        |
| 3   | RS-c  | 180×120×4.63                        | 30×1.94                  | 0.142      | 30.8%  | 90            | 0.50  | 334.8             | 371.8             | 49.8              | 79.3                | 2261.8                        |
| 4   | RC-a  | 180×120×2.68                        | 33×1.97                  | 0.079      | 29.2%  | 87            | 0.48  | 324.9             | 352.9             | 49.8              | 52.3                | 1453.7                        |
| 5   | RC-b  | 180×120×3.66                        | 33×1.97                  | 0.110      | 29.6%  | 87            | 0.48  | 333.7             | 352.9             | 49.8              | 59.1                | 1919.1                        |
| 6   | RC-c  | 180×120×4.63                        | 33×1.97                  | 0.142      | 30.0%  | 87            | 0.48  | 334.8             | 352.9             | 49.8              | 81.4                | 2171.1                        |

**Table 2.** Properties of steel tubes.

| Type       | Cross-section | $t_o(t_i)$<br>(mm) | Yield strength<br>(MPa) | Tensile strength<br>(MPa) | Elastic modulus<br>(N/mm <sup>2</sup> ) | Poisson's ratio | Elongation<br>(%) |
|------------|---------------|--------------------|-------------------------|---------------------------|---|-----------------|-------------------|
| Outer tube | Rectangular   | 2.68               | 324.9                   | 462.6                     | $2.03 \times 10^5$                      | 0.273           | 27.2              |
|            |               | 3.66               | 333.7                   | 452.0                     | $2.06 \times 10^5$                      | 0.292           | 28.7              |
|            |               | 4.63               | 334.8                   | 468.2                     | $2.03 \times 10^5$                      | 0.277           | 32.3              |
| Inner tube | Square        | 1.94               | 371.8                   | 460.9                     | $1.92 \times 10^5$                      | 0.278           | 14.6              |
|            | Circular      | 1.97               | 352.9                   | 451.2                     | $1.88 \times 10^5$                      | 0.270           | 15.4              |

**Table 3.** Plasticity parameters for CDP model

| Plasticity parameter | Dilation angle | Flow potential eccentricity | Ratio of $\sigma_{b0}$ to $\sigma_{c0}$ | Ratio of $q_{(TM)}$ to $q_{(CM)}$ | Viscosity parameter |
|----------------------|----------------|-----------------------------|---|-----------------------------------|---------------------|
| Value                | 30°            | 0.1                         | 1.16                                    | 2/3                               | $5 \times 10^{-6}$  |

Note:  $\sigma_{b0}$  is initial equibiaxial compressive yield stress,  $\sigma_{c0}$  is initial uniaxial compressive yield stress, and  $q_{(TM)}$  and  $q_{(CM)}$  are the second stress invariant on the tensile and compressive meridian, respectively.